LAWRENCE
LIVERMORE
NATIONAL
LABORATORY

LLNL-JRNL-2010906-DRAFT

# A Hybrid Monte Carlo-Deterministic Second Moment Method with Efficient Variance Reduction

M. M. Pozulp, T. S. Haut, P. S. Brantley,
S. S. Olivier

September 4, 2025

## Disclaimer



This work performed under the auspices of the U.S. Department of Energy by Lawrence Livermore National Laboratory under Contract DE-AC52-07NA27344.

# A Hybrid Monte Carlo-Deterministic Second Moment Method with Efficient Variance Reduction

Michael Pozulp[a,*], Terry Haut[b], Patrick Brantley[c], Samuel Olivier[d]

[a]*Lawrence Livermore National Laboratory, Applications, Simulations, and Quality Division, Livermore, California 94550*
[b]*Lawrence Livermore National Laboratory, Center for Applied Scientific Computing, Livermore, California 94550*
[c]*Lawrence Livermore National Laboratory, Design Physics Division, Livermore, California 94550*
[d]*Los Alamos National Laboratory, Computer, Computational, and Statistical Sciences Division, Los Alamos, New Mexico 87545*

**Abstract**

We present a hybrid method that combines Monte Carlo with deterministic finite element methods to solve a linear Boltzmann transport equation. Our hybrid method runs orders of magnitude faster than Monte Carlo, without sacrificing accuracy, for a proxy problem from radiative transfer that contains both optically-thick and optically-thin material. We believe that this is the first demonstration of a hybrid Second Moment Method in more than one spatial dimension, the first to consider more than one material, and the first to use variance reduction. Our variance reduction approach arises from an asymptotic analysis in which we show that the magnitude of the scattering source grows without bound. We transform the problem to compute the deviation of the radiation intensity from isotropy. The magnitude of the source in the transformed problem is bounded, and the quality of the hybrid method solution is dramatically improved by a substantial reduction in the variance.

*Keywords:* Second Moment Method, Monte Carlo, Variance Reduction

## 1. Introduction

The Second Moment Method (SMM) is an iterative method which solves a linear Boltzmann transport equation and a system of linear moment equations every cycle [1]. The transport equation and the moment equations are coupled through source terms. The linearity and source coupling of SMM contrasts with the non-linearity and operator coupling of Quasidiffusion, or Variable Eddington Factor (VEF) [2]. SMM and VEF converge quickly in the optically-thick, highly-scattering transport regime known as the thick diffusion limit (TDL) [3]. Source iteration (SI), which lags the scattering source in order to avoid forming the transport operator, converges arbitrarily slowly in the TDL. Methods such as diffusion synthetic acceleration (DSA) accelerate SI convergence [4]. SMM and VEF are similar to DSA, in the sense that all three methods converge quickly, but there are some important differences. For example, the low-order problem must be "consistent" with the high-order problem for DSA to always converge quickly [5].

Our hybrid method lags the scattering source, not to avoid forming the transport operator, but to avoid simulating scattering events in the Monte Carlo particle histories. Simulating these events can dominate the calculation runtime in the TDL. However, just like SI with deterministic methods, Monte Carlo SI converges arbitrarily slowly in the TDL. We fix this problem by creating a hybrid SMM that converges quickly. We use SMM instead of DSA because our use of Monte Carlo to solve the high-order problem makes it unclear how we would satisfy the consistency requirement. We chose SMM over VEF because of statistical variation—hereafter referred to as noise—which could be more complicated to manage when it appears in the operator, as in hybrid VEF, rather than in the source, as in hybrid SMM. We use Monte Carlo because it allows the

*Corresponding author

dimensions of the high-order problem to remain continuous, thereby avoiding discretization errors such as the unphysical starburst patterns known as "ray effects" that are caused by angular under-resolution.

Using Monte Carlo (MC) introduces noise, which can diminish the accuracy of MC estimators to the extent that the estimates become worthless. Hybrid methods may amplify this noise through differentiation. We avoid noise amplification by solving the first-order form of the low-order problem, which involves only a single spatial derivative acting on the noisy source term, and we use integration by parts with a finite element method to transfer the derivative from the noisy source term to a test function in the weak formulation. Although the interior face terms in the weak form could be calculated using surface estimators, we instead use volumetric estimators and apply finite element interpolation to evaluate these terms in the weak form. Numerical evidence suggests that solving the weak, first-order form without surface estimators is sufficient for avoiding noise amplification.

However, we found that simply avoiding noise amplification is not sufficient to provide an efficient hybrid alternative to Monte Carlo for calculations in the previously mentioned TDL regime. To address this issue, we perform an asymptotic analysis to derive an expression relating the variance of the MC estimators in our hybrid method to $\epsilon$, the parameter characterizing the TDL. Our analysis demonstrates that, without variance reduction designed specifically to alleviate the undesirable dependency of the variance on the parameter $\epsilon$, the solution of *any* Monte Carlo source iteration method will be arbitrarily noisy in the TDL. Therefore, we develop and implement a variance reduction technique that transforms the high-order problem into one that requires computing the deviation of the radiation intensity from isotropy. In the transformed problem, the variance of the MC estimators limits to zero, rather than infinity, in the TDL.

The transformed problem resembles the difference formulation, which considers the deviation of the intensity from the Planck distribution [6]. As a result, the material emission source is replaced by the space-time derivative of the Planck function. The spatial gradient term in the inhomogeneous source of the difference formulation can be addressed by sourcing MC particles on the interior faces of the mesh [7]. A notable feature of our hybrid method is that we do not use interior face sources, despite a similar gradient appearing in our inhomogeneous source term. Although this approach is possible within our hybrid method—and would require sourcing only on the interior mesh faces that coincide with material interfaces—we instead apply finite element differentiation to compute a volumetric source which we sample instead of face sources. Our technique is an extension of the difference formulation to iterative Monte Carlo, and the resulting equations in the high-order problem resemble those in the generalized difference formulation [8].

An example of an issue that our hybrid method could fix, were it to be extended to nonlinear transport, is the very long runtimes of Monte Carlo calculations which solve the thermal radiative transfer (TRT) equations using Fleck & Cummings' "implicit Monte Carlo" (IMC) linearization [9]. The IMC linearization produces a linear transport equation with an effective scattering source which causes arbitrarily long IMC photon histories in the TDL, leading to arbitrarily long IMC calculation runtimes. Fleck & Canfield's Random Walk (RW) algorithm can reduce the runtime by replacing many steps with a single step in the histories of IMC photons which satisfy certain properties [10]. The equation that we solve is linear, unlike TRT, but it still reproduces the long IMC runtime issue.

Runtime improvements exceeding that of RW can be achieved using more recently developed IMC acceleration algorithms, such as implicit Monte Carlo Diffusion (IMD) [11, 12] or discrete diffusion Monte Carlo (DDMC) [13, 14]. IMD and DDMC are very effective, but not perfect. Both algorithms use diffusion approximations, require phase-space partitioning, and have not been extended to meshes with reentrant elements. In contrast, our method does not use diffusion, does not partition phase-space, and does not have issues with reentrant elements. Reentrant elements can arise in radiation-hydrodynamics calculations when the Lagrangian hydrodynamic frame is employed—for example, when a mesh of squares is distorted by fluid flow, resulting in a quadrilateral mesh that contains darts, which are elements shaped like arrow heads.

Although we suggest thermal radiative transfer as an application of our method, we make no assumptions about the type of particle in the simulation—our method is applicable as long as the linear transport equation under consideration is a valid physical model for the particle type. Neutrons, like photons, can be simulated in accordance with a linear transport equation. One example of a problem that our hybrid method could address in neutronics calculations is slow Monte Carlo neutron transport simulation runtimes resulting from the long histories of MC neutrons traversing optically thick, highly scattering materials, such as the

moderator surrounding the core in a nuclear power reactor.

SMM and VEF algorithms typically use deterministic methods to solve both the high-order transport problem and the low-order moment system. We use the term "hybrid" because our method employs Monte Carlo to solve the high-order problem. We believe that our method is the first demonstration of a hybrid SMM in more than one spatial dimension, the first to consider more than one material, and the first to use variance reduction. However, a few similar hybrid methods exist. These can be grouped into two categories: those that interrupt a Monte Carlo calculation one or more times to solve a moment system without actually iterating, and those that iterate to converge quantities such as a source term or the Eddington tensor.

The "interrupt" category of similar hybrid methods contains what may be the earliest example of a hybrid SMM or VEF method: Cooper & Larsen's method to compute weight windows to reduce the variance of a Monte Carlo calculation [15]. By interrupting their MC calculation to solve a VEF system, then using the VEF system solution to set weight windows before resuming their MC calculation, Cooper & Larsen reduced the variance of their MC solution, while also improving an important Monte Carlo figure of merit. More recently, Novellino & Anistratov computed MC solutions for a transport problem, followed by SMM and VEF system solutions, and found that the moment system solutions were sometimes more accurate than the MC solution [16].

The category of similar hybrid methods which iterate is larger than the "interrupt" category. Willert et al. replaced the deterministic transport solve in a method that uses nonlinear diffusion acceleration (NDA) with Jacobian-free Newton-Krylov (JFNK) to accelerate source iteration in a method called JFNK-NDA(MC) [17]. Park et al. created a hybrid method by using Monte Carlo with the moment method that they described in [18]. In their hybrid method, Park et al. use MC to compute consistency terms which appear in their moment system [19]. They also use phase-space partitioning in a similar manner to IMD and DDMC. Lam et al. linearized the TRT equations in a way that avoids effective scattering, then solved a transport equation using Monte Carlo and a diffusion equation using a finite element method to converge a Newton iteration [20]. Pasmann et al. used a low-discrepancy sequence instead of a pseudo-random number sequence to improve the asymptotic order of the estimator uncertainty such that a factor of two reduction in the uncertainty requires only twice as many particles, instead of four times as many. This enhancement violates assumptions which allow for the contribution of the scattering and fission sources to be included through scattering events and fission events. Pasmann et al. accounts for the contribution in the particle weights, and re-computes the contribution every cycle of an iteration [21].

We refer to our method as hybrid second moment (HSM), and in the next section we describe HSM without any derivations. The purpose of the section is to summarize the method before showing details, such as derivations, which we include in subsequent sections. In addition to derivations, we provide an analysis of the MC estimator variance in the TDL. After describing some details of our implementation, we then show numerical results which demonstrate that HSM is orders of magnitude faster than Monte Carlo, without sacrificing accuracy, for a proxy problem from radiative transfer that contains both optically-thick and optically-thin material. We conclude with a summary and suggestions for future work.

## 2. Hybrid Second Moment Algorithm

A steady-state, gray, linear Boltzmann transport equation may be written,

$$\boldsymbol{\Omega} \cdot \nabla \psi + \sigma_t \psi = \frac{\sigma_s}{4\pi} \int_{\mathbb{S}^2} \psi \, \mathrm{d}\Omega' + q \,, \tag{1a}$$

where $\boldsymbol{\Omega} \in \mathbb{S}^2$ is the unit direction vector, $\mathbb{S}^2$ is the unit sphere, $\psi$ is the radiation intensity, $\sigma_t$ is the total material opacity, $\sigma_s$ is the scattering opacity, and $q$ is an arbitrary source function. Equation (1a) is subject to an inflow boundary condition, which defines the radiation intensity on the domain boundary in the hemisphere of directions that point into the domain at a given location on the domain boundary surface,

$$\psi(\mathbf{x}, \boldsymbol{\Omega}) = \psi_{\mathrm{inc}}(\mathbf{x}, \boldsymbol{\Omega}) \,, \quad \mathbf{x} \in \partial\mathcal{D} \text{ and } \boldsymbol{\Omega} \cdot \mathbf{n} < 0 \,, \tag{1b}$$

where $\mathbf{x} \in \mathbb{R}^{\dim}$ is the spatial position coordinate, $\psi_{\text{inc}}$ is an arbitrary inflow function, $\partial\mathcal{D}$ is the domain boundary, and $\mathbf{n}$ is the outward facing unit normal vector on the domain boundary surface. The second moment system associated with the linear transport problem can be derived by taking angular moments of eq. (1a). A boundary condition for the system can be derived by manipulating partial currents. The second moment system is (see section 3 for the derivation),

$$\nabla \cdot \boldsymbol{J} + \sigma_a \varphi = Q_0 \,, \qquad \mathbf{x} \in \mathcal{D} \,, \tag{2a}$$

$$\frac{1}{3}\nabla\varphi + \sigma_t \boldsymbol{J} = \boldsymbol{Q}_1 - \nabla \cdot \mathbf{T} \,, \quad \mathbf{x} \in \mathcal{D} \,, \tag{2b}$$

$$\boldsymbol{J} \cdot \mathbf{n} = \frac{1}{2}\varphi + 2J_{\text{in}} + \beta \,, \qquad \mathbf{x} \in \partial\mathcal{D} \,, \tag{2c}$$

where $\boldsymbol{J} \in \mathbb{R}^{\dim}$ is the vector unknown, $\sigma_a = \sigma_t - \sigma_s$ is the absorption opacity, $\varphi$ is the scalar unknown, $Q_0$ is the zeroth angular moment of $q$, $\boldsymbol{Q}_1$ is the first angular moment of $q$, $J_{\text{in}}$ is a functional of $\psi_{\text{inc}}$, and $\mathbf{T}$ and $\beta$ functionals of $\psi$. The functionals are,

$$J_{\text{in}} = \int_{\boldsymbol{\Omega}\cdot\mathbf{n}<0} \boldsymbol{\Omega} \cdot \mathbf{n}\, \psi_{\text{inc}} \, \mathrm{d}\Omega \,, \tag{3}$$

$$\mathbf{T} = \int_{\mathbb{S}^2} \boldsymbol{\Omega} \otimes \boldsymbol{\Omega}\, \psi \, \mathrm{d}\Omega - \frac{1}{3}\mathbf{I} \int_{\mathbb{S}^2} \psi \, \mathrm{d}\Omega \,, \tag{4}$$

$$\beta(\psi) = \int_{\mathbb{S}^2} |\boldsymbol{\Omega} \cdot \mathbf{n}|\, \psi \, \mathrm{d}\Omega - \frac{1}{2}\int_{\mathbb{S}^2} \psi \, \mathrm{d}\Omega \,, \tag{5}$$

where $\mathbf{I}$ is the identity matrix. When $\mathbf{T}$ and $\beta$ are zero, the system of eqs. (2a) and (2b) simplifies to the radiation diffusion approximation, and eq. (2c) simplifies to the Marshak boundary condition. For this reason, we refer to $\mathbf{T} \in \mathbb{R}^{\dim \times \dim}$ as the transport correction tensor and $\beta$ as the boundary correction factor. While $\mathbf{T}$ has nine entries when $\dim = 3$, only six are unique, because $\mathbf{T}$ is symmetric. Before discretization, eqs. (2a) to (2c) are an equivalent reformulation of eqs. (1a) and (1b). Thus, before discretization, the scalar and vector unknowns in the SMM system are equal to the zeroth and first angular moments of the intensity.

The Second Moment Method uses $\varphi$, which comes from solving the moment system, to compute the scattering source in eq. (1a). We write this by simply replacing the angle integrated intensity in eq. (1a) with $\varphi$,

$$\boldsymbol{\Omega} \cdot \nabla\psi + \sigma_t\psi = \frac{\sigma_s}{4\pi}\varphi + q \,. \tag{6}$$

Solving eq. (6) along with the boundary condition eq. (1b) for $\psi$ allows us to compute the SMM data $\mathbf{T}$ and $\beta$, which are functionals of $\psi$. Figure 1 shows the SMM iteration. In our hybrid method, we may use Monte Carlo without scattering events to solve the linear transport equation (left side of fig. 1) and compute the SMM data $\mathbf{T}$ and $\beta$ as Monte Carlo estimators. We may then solve the moment system (right side of fig. 1) using a deterministic method, and use the solution $\varphi$ to compute the scattering source, which we converge in an iteration.

However, such a hybrid method would have a Monte Carlo solution estimator with an arbitrarily large variance in the TDL. Specifically, the variance would be $O(1/\epsilon)$, where $\epsilon \in (0, 1]$ is the TDL parameter, and $\epsilon \to 0$ defines the TDL. To fix the noise issue, we must fix the undesirable dependence of the variance on $\epsilon$. We do this by substituting $\psi = \bar{\varphi}/(4\pi) + \tilde{\psi}$ into eq. (6), where $\tilde{\psi}$ is a new unknown quantity representing the amount by which the intensity $\psi$ deviates from $\bar{\varphi}/(4\pi)$, and $\bar{\varphi}$ is an arbitrary function which we leave undefined for now. The result of the substitution is,

$$\boldsymbol{\Omega} \cdot \nabla\tilde{\psi} + \sigma_t\tilde{\psi} = \frac{\sigma_t}{4\pi}(\varphi - \bar{\varphi}) - \frac{1}{4\pi}(\sigma_a\varphi + \boldsymbol{\Omega} \cdot \nabla\bar{\varphi}) + q \,. \tag{7a}$$

Making the same substitution into eq. (1b) gives the new inflow boundary condition,

$$\tilde{\psi}(\mathbf{x}, \boldsymbol{\Omega}) = \psi_{\text{inc}}(\mathbf{x}, \boldsymbol{\Omega}) - \frac{1}{4\pi}\bar{\varphi}(\mathbf{x}) \,, \quad \mathbf{x} \in \partial\mathcal{D} \text{ and } \boldsymbol{\Omega} \cdot \mathbf{n} < 0 \,. \tag{7b}$$

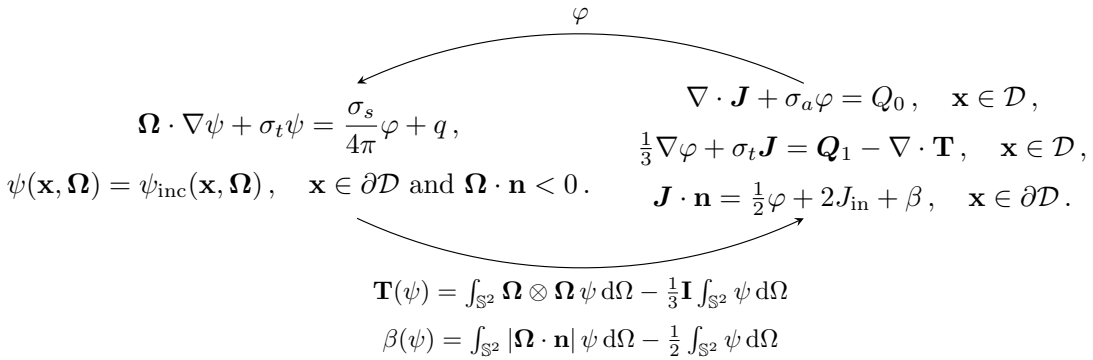


Figure 1: SMM algorithm.

How do we choose the arbitrary function $\bar{\varphi}$ in the transformed problem defined by eqs. (7a) and (7b)? We need $\varphi - \bar{\varphi}$ to be $O(1/\sigma_t)$ in order to fix the noise issue because of how the variance depends on the total source function, which we will show in section 4.1. A simple choice would be $\bar{\varphi} = \varphi$. We could make this choice, and then account for the $\nabla\varphi$ source term by sourcing MC particles on the material interfaces. In a mesh where material interfaces coincide with interior mesh faces, and each mesh element contains a different material, this would require sourcing MC particles on every interior mesh face.

Our approach avoids interior face sources by applying finite element differentiation to compute a volumetric source that we sample instead of face sources. We choose $\bar{\varphi} \neq \varphi$ in order to avoid computing $\nabla\varphi$, which would introduce a well-posedness issue. This is because the solution of the transport equation is generally not differentiable, and so approximating the derivative of the transport solution will not give convergence no matter what numerical scheme is used. The formulation itself is not well-posed. Thus, we choose $\bar{\varphi}$ such that it satisfies the following conditions,

1. $\nabla\bar{\varphi}$ is well-defined, and
2. $\varphi - \bar{\varphi}$ is $O(1/\sigma_t)$.

Numerical evidence suggests that the first condition is necessary for our hybrid method to converge to the correct solution in portions of phase space where the gradient of the transport solution may not be well-defined, such as on material interfaces. The second condition fixes the noise issue by causing the MC estimator variance to be $O(\epsilon)$ instead of $O(1/\epsilon)$. Choosing $\bar{\varphi} = \varphi$ would satisfy the second condition, but not the first. We satisfy both conditions by solving a transient heat conduction equation for $\bar{\varphi}$,

$$\frac{\partial\bar{\varphi}}{\partial t} = \nabla \cdot \frac{1}{\sigma_t}\nabla\bar{\varphi}, \quad \mathbf{x} \in \mathcal{D}\,. \tag{8a}$$

Equation (8a) satisfies the first condition because it tends to produce differentiable solutions. This is true even when the initial condition is not differentiable, as in our case, because we use $\varphi$ as the initial data:

$$\bar{\varphi}(\mathbf{x}, 0) = \varphi(\mathbf{x}), \quad \mathbf{x} \in \mathcal{D}\,. \tag{8b}$$

We satisfy the second condition by employing the following three techniques: i) choosing $1/\sigma_t$ for the conduction coefficient in eq. (8a), ii) choosing a Dirichlet boundary condition with $\varphi$ as the Dirichlet data,

$$\bar{\varphi}(\mathbf{x}, t) = \varphi(\mathbf{x}), \quad \mathbf{x} \in \partial\mathcal{D}\,, \tag{8c}$$

and iii) computing a single timestep of backward Euler where the timestep size is subject to the limitation,

$$\frac{\Delta t}{h^2}\frac{1}{\max_{\mathbf{x}}\sigma_t} \ll 1\,. \tag{9}$$

Figure 2 shows the resulting HSM algorithm. The second moment system in the HSM algorithm remains unchanged from the SMM algorithm (see fig. 1). However, the transport equations differ, and the HSM algorithm has an additional transient heat conduction solve. We use Monte Carlo to solve the transport equation and a deterministic method to solve the moment system and the conduction equation. Monte Carlo avoids the ray effects which can appear in deterministic methods, such as discrete ordinates ($\mathrm{S}_N$), due to under-resolution in angle. The moment system and the conduction equation do not depend on angle.

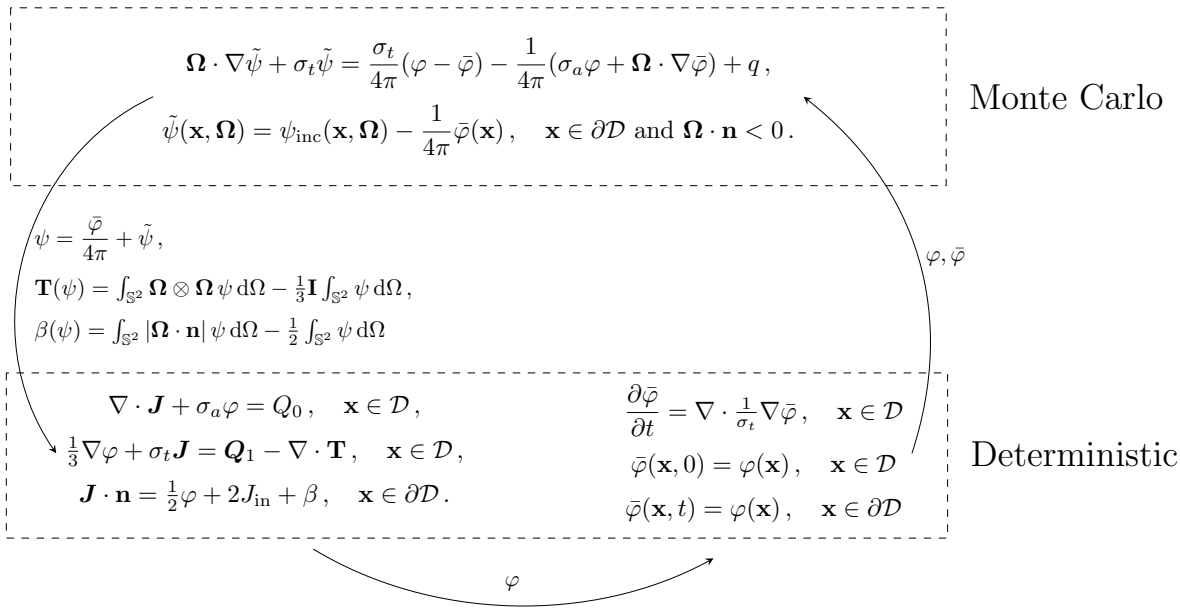


Figure 2: Hybrid second moment (HSM) algorithm.

Algorithm 1 shows pseudocode for the HSM algorithm, in which $\hat{\phi}$ is a MC estimator of the angle integrated intensity,

$$\phi=\int_{\mathbb{S}^2}\psi\,\mathrm{d}\boldsymbol{\Omega}\,, \tag{10}$$

and $\hat{\mathbf{T}}$ and $\hat{\beta}$ are MC estimators of $\mathbf{T}$ and $\beta$, respectively. The first MC transport solve uses the fixed source functions $q$ and $\psi_{\mathrm{inc}}$, whereas the subsequent MC transport solves use $\varphi^{(i)}$ and $\bar{\varphi}^{(i)}$, which are necessary to form the variable source functions. This allows us to use all of the particle memory to sample the fixed sources before iterating, then re-use all of the particle memory to sample the variable sources during the iteration. The iteration converges when the relative difference of successive iterates falls below a user-provided threshold $\eta$,

$$\max_j\left(\frac{|\hat{\phi}_j^{(i-1)}-\hat{\phi}_j^{(i)}|}{\hat{\phi}_j^{(i-1)}}\right)<\eta\,,\qquad j=1,\ldots,|\mathcal{T}|\,, \tag{11}$$

where $|\mathcal{T}|$ is the number of elements in the mesh. In algorithm 1, we recompute the particle weights every cycle, but the other parameters of the particles, as well as their histories, remain unchanged. We achieve this by resetting the pseudo-random number generator seed every cycle of the HSM iteration (see fig. 3). Finally, recall that the HSM method for solving eqs. (1a) and (1b) does not include scattering events. Thus, the histories of the particles in the MC transport solves in algorithm 1 do not include scattering events. The histories consist of a sequence of zero or more facet crossings terminated with absorption or leakage. The combination of having no scattering events, which allows each cycle to be computed quickly, and robust convergence, which ensures that only a few iterations—ten or fewer in all the calculations presented here—are required for convergence, makes HSM an effective algorithm for linear transport.

**Algorithm 1** Hybrid Second Moment

$\hat{\phi}^{(0)}, \hat{\mathbf{T}}^{(0)}, \hat{\beta}^{(0)} \leftarrow$ mc_transport_solve($q$, $\psi_{\text{inc}}$)
$i \leftarrow 1$
**while** not converged($\hat{\phi}^{(i-1)}, \hat{\phi}^{(i)}$) **do**
    $\varphi^{(i)} \leftarrow$ second_moment_system_solve($Q_0, \boldsymbol{Q}_1, \hat{\mathbf{T}}^{(i-1)}, \hat{\beta}^{(i-1)}$)
    $\bar{\varphi}^{(i)} \leftarrow$ transient_heat_conduction_solve($\varphi^{(i)}$)
    $\hat{\phi}_{\text{temp}}, \hat{\mathbf{T}}_{\text{temp}}, \hat{\beta}_{\text{temp}} \leftarrow$ mc_transport_solve($\varphi^{(i)}$, $\bar{\varphi}^{(i)}$)
    $\hat{\phi}^{(i)} \leftarrow \hat{\phi}^{(0)} + \hat{\phi}_{\text{temp}}$
    $\hat{\mathbf{T}}^{(i)} \leftarrow \hat{\mathbf{T}}^{(0)} + \hat{\mathbf{T}}_{\text{temp}}$
    $\hat{\beta}^{(i)} \leftarrow \hat{\beta}^{(0)} + \hat{\beta}_{\text{temp}}$
    $i \leftarrow i + 1$
**return** $\hat{\phi}^{(i)}$

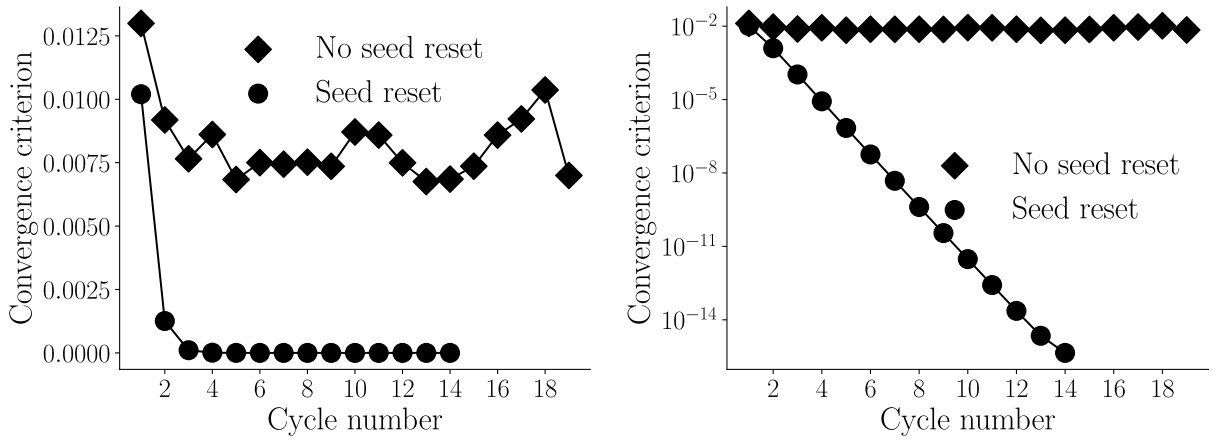


(a) Linear vertical axis.

(b) Logarithmic vertical axis.

Figure 3: Resetting the pseudo-random number generator seed allows the HSM iteration to converge to machine precision for the convergence criterion specified in eq. (11). The information content of each particle history would be greater if the seed were not reset. However, this approach would require a more sophisticated convergence criterion which depends on more than just the current and previous iterates. For example, neutronics eigenvalue iteration algorithms typically do not reset the seed and often compute a moving average of iterates to assess convergence.

## 3. Deterministic Component of HSM

In this section, we derive the second moment system of eqs. (2a) and (2b) and the boundary condition eq. (2c). We use a finite element method to solve the second moment system, as well as the transient heat conduction eq. (8a), which we describe after presenting the weak form for each.

### *3.1. Derivation of the Second Moment System*

We derive the second moment system of eqs. (2a) and (2b) and the boundary condition eq. (2c) following the procedure in Olivier and Haut [22]. Define the zeroth, first, and second angular moments of the radiation intensity $\psi$,

$$\phi(\mathbf{x}) = \int_{\mathbb{S}^2} \psi(\mathbf{x}, \boldsymbol{\Omega}) \, \mathrm{d}\Omega \,, \tag{12}$$

$$\boldsymbol{J}(\mathbf{x}) = \int_{\mathbb{S}^2} \boldsymbol{\Omega} \, \psi(\mathbf{x}, \boldsymbol{\Omega}) \, \mathrm{d}\Omega \,, \tag{13}$$

$$\mathbf{P}(\mathbf{x}) = \int_{\mathbb{S}^2} \mathbf{\Omega} \otimes \mathbf{\Omega}\, \psi(\mathbf{x}, \mathbf{\Omega})\, \mathrm{d}\Omega\,. \tag{14}$$

Define the zeroth and first angular moments of the arbitrary source function $q$,

$$Q_0(\mathbf{x}) = \int_{\mathbb{S}^2} q(\mathbf{x}, \mathbf{\Omega})\, \mathrm{d}\Omega\,, \tag{15}$$

$$\boldsymbol{Q}_1(\mathbf{x}) = \int_{\mathbb{S}^2} \mathbf{\Omega}\, q(\mathbf{x}, \mathbf{\Omega})\,. \tag{16}$$

Taking the zeroth and first angular moments of eq. (1a) gives,

$$\nabla \cdot \boldsymbol{J} + \sigma_a \phi = Q_0\,, \tag{17a}$$

$$\nabla \cdot \mathbf{P} + \sigma_t \boldsymbol{J} = \boldsymbol{Q}_1\,. \tag{17b}$$

The system of eqs. (17a) and (17b) is unclosed because it has ten unknowns and only four equations when three spatial dimensions are considered. In 3D, the independent variables $\phi$, $\boldsymbol{J}$, and $\mathbf{P}$ consist of 1+3+6=10 unknowns because they are a scalar, vector, and symmetric tensor, respectively; eq. (17a) is one equation, and eq. (17b) is three. The exact closure which defines the Second Moment Method (SMM) is,

$$\mathbf{P} = \mathbf{T} + \frac{1}{3}\mathbf{I}\phi\,, \tag{18}$$

where $\mathbf{T}$ is defined in eq. (4) and $\mathbf{I}$ is the identity matrix.

We derive a boundary condition by defining partial currents,

$$J_n^{\pm} = \int_{\mathbf{\Omega}\cdot\mathbf{n} \gtrless 0} \mathbf{\Omega} \cdot \mathbf{n}\, \psi\, \mathrm{d}\Omega\,, \tag{19}$$

and performing algebraic manipulation,

$$\begin{aligned} \boldsymbol{J} \cdot \mathbf{n} &= J_n^- + J_n^+ \\ &= 2J_n^- + (J_n^+ - J_n^-) \\ &= 2J_n^- + \int_{\mathbb{S}^2} |\mathbf{\Omega} \cdot \mathbf{n}|\, \psi\, \mathrm{d}\Omega\,. \end{aligned} \tag{20}$$

Defining the quantity,

$$B(\psi) = \int_{\mathbb{S}^2} |\mathbf{\Omega} \cdot \mathbf{n}|\, \psi\, \mathrm{d}\Omega\,, \tag{21}$$

and using $J_{\text{in}}$ as defined in eq. (3) allows us to write the unclosed boundary condition,

$$\boldsymbol{J} \cdot \mathbf{n} = B(\psi) + 2J_{\text{in}}\,. \tag{22}$$

The exact closure for eq. (22) which defines the SMM is,

$$B = \beta + \frac{1}{2}\phi\,, \tag{23}$$

where $\beta$ is defined in eq. (5). Substituting the exact SMM closure eq. (18) into eq. (17b), and the exact SMM closure eq. (23) into eq. (22) gives the second moment system of eqs. (2a) and (2b) and the boundary condition eq. (2c). Note that we switched from using $\phi$ in eqs. (17a), (18) and (23) to $\varphi$ in eqs. (2a) to (2c) to emphasize that, even though the second moment system is an equivalent reformulation of the transport equation, $\varphi$ can differ from the $\phi$ defined in eq. (12) after discretization, which is the case for our HSM method.

*3.2. Mixed Finite Element Method for Solving the Second Moment System*

The key consideration when solving the second moment system in our hybrid method is to avoid amplifying the noise in the SMM data, $\mathbf{T}$ and $\beta$. Computing $\mathbf{T}$ and $\beta$ using Monte Carlo introduces noise, and differentiating a noisy quantity tends to amplify the noise. This suggests that we should solve the first order form of the system. Additionally, numerical evidence suggests that we should solve a weak form of eq. (2b) so that we can replace the strong derivative on $\mathbf{T}$ with a weak derivative. We use finite elements to discretize space, and integration by parts to move the derivative from $\mathbf{T}$ to the test function. Integration by parts generates interior face integrals that we compute without interior face estimators. Instead, we use finite element interpolation of a volume estimator of $\mathbf{T}$ to compute $\mathbf{T}$ on the interior faces. Other approaches might also avoid noise amplification, and some may do so more efficiently; however, ours is a sufficient approach to avoid it.

The first order form is a mixed problem, which requires simultaneously solving for two quantities that belong to different finite element spaces. The FEM weak form for the mixed problem is: find $(\varphi, \boldsymbol{J}) \in Y_1 \times RT_0$ such that,

$$\int u \nabla \cdot \boldsymbol{J} \,\mathrm{d}\mathbf{x} + \int \sigma_a \, u\varphi \,\mathrm{d}\mathbf{x} = \int u \, Q_0 \,\mathrm{d}\mathbf{x}\,, \quad \forall u \in Y_1\,, \tag{24a}$$

$$-\frac{1}{3}\int \nabla \cdot \boldsymbol{v}\, \varphi \,\mathrm{d}\mathbf{x} + \int \sigma_t \, \boldsymbol{v} \cdot \boldsymbol{J} \,\mathrm{d}\mathbf{x} + \frac{2}{3}\int_{\Gamma_b} (\boldsymbol{v}\cdot\mathbf{n})(\boldsymbol{J}\cdot\mathbf{n})\,\mathrm{d}s = \int \boldsymbol{v}\cdot\boldsymbol{Q}_1 \,\mathrm{d}\mathbf{x} - \int_{\Gamma_b} \boldsymbol{v}\cdot\mathbf{T}\mathbf{n}\,\mathrm{d}s$$
$$+\frac{2}{3}\int_{\Gamma_b} (\boldsymbol{v}\cdot\mathbf{n})(2J_{\text{in}} + \beta)\,\mathrm{d}s - \int_{\Gamma_0} [\![v]\!]\cdot\{\!\{\mathbf{T}\mathbf{n}\}\!\}\,\mathrm{d}s + \int \nabla_h \boldsymbol{v} : \mathbf{T}\,\mathrm{d}\mathbf{x} \quad \forall \boldsymbol{v} \in RT_0\,. \tag{24b}$$

In eqs. (24a) and (24b), $\varphi$ and $\boldsymbol{J}$ are the scalar and vector trial functions, respectively, $u$ and $\boldsymbol{v}$ are the scalar and vector test functions, respectively, and $Y_1$ and $RT_0$ are the degree-1 Discontinuous Galerkin (DG) and degree-0 Raviart Thomas (RT) finite element spaces, respectively [23, 24]. Figure 4 shows the locations of the $Y_1$ and $RT_0$ degrees of freedom on the unit square.

The "broken" gradient $\nabla_h$, the jump operator $[\![\cdot]\!]$, and the average operator $\{\!\{\cdot\}\!\}$ are defined as,

$$(\nabla_h u)|_K = \nabla(u|_K) \;\; \forall K \in \mathcal{T}\,, \tag{25}$$

$$[\![u]\!] = \begin{cases} u_1 - u_2 & \mathcal{F} \in \Gamma_0 \\ u & \mathcal{F} \in \Gamma_b \end{cases}, \tag{26}$$

$$\{\!\{u\}\!\} = \begin{cases} \dfrac{u_1 + u_2}{2} & \mathcal{F} \in \Gamma_0 \\ u & \mathcal{F} \in \Gamma_b \end{cases}, \tag{27}$$

where $K$ is an element in the mesh, $\mathcal{T}$ is the set of all mesh elements, $\mathcal{F}$ is a mesh element face, $\Gamma_0$ is the set of unique faces on the interior of the mesh, and $\Gamma_b$ is the set of unique faces on the boundary of the mesh.

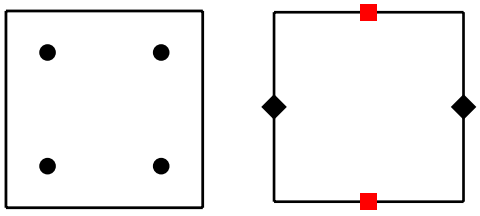

(a) $Y_1$ (b) $RT_0$

Figure 4: Location of the degrees of freedom for the (a) $Y_1$ and (b) $RT_0$ finite element spaces on a square element. In (b), the black diamonds and red squares denote degrees of freedom representing the $x$ and $y$ components, respectively.

To derive eq. (24a), let $u \in Y_1$, multiply eq. (2a) by $u$, then integrate over $\mathcal{D}$. Deriving eq. (24b) requires several steps and employs integration by parts rules created using the following vector calculus identities:

- Product rule for divergence of a scalar ($a$) times a vector ($\boldsymbol{F}$):

$$\nabla \cdot (a\boldsymbol{F}) = \nabla a \cdot \boldsymbol{F} + a\nabla \cdot \boldsymbol{F}\,, \tag{28}$$

- Divergence theorem:

$$\int_K \nabla \cdot \boldsymbol{F}\,\mathrm{d}\mathbf{x} = \int_{\partial K} \boldsymbol{F} \cdot \mathbf{n}\,\mathrm{d}s\,, \tag{29}$$

- Product rule for divergence of a vector ($\boldsymbol{v}$) dotted with a tensor ($\mathbf{T}$):

$$\nabla \cdot (\boldsymbol{v} \cdot \mathbf{T}) = \boldsymbol{v} \cdot (\nabla \cdot \mathbf{T}) + \mathbf{T} : \nabla \boldsymbol{v}\,, \tag{30}$$

- Double dot product involving vectors ($\boldsymbol{v}$, $\mathbf{n}$) and a tensor ($\mathbf{T}$):

$$(\boldsymbol{v} \cdot \mathbf{T}) \cdot \mathbf{n} = \boldsymbol{v} \cdot (\mathbf{T}\mathbf{n})\,. \tag{31}$$

Combining eq. (28) with eq. (29) gives an integration by parts rule,

$$\int \nabla a \cdot \boldsymbol{F}\,\mathrm{d}\mathbf{x} = -\int a\nabla \cdot \boldsymbol{F}\,\mathrm{d}\mathbf{x} - \int_{\partial K} a(\boldsymbol{F} \cdot \mathbf{n})\,\mathrm{d}s\,. \tag{32}$$

Combining eqs. (28) to (30) gives another integration by parts rule,

$$\int \boldsymbol{v} \cdot \nabla \cdot \mathbf{T}\,\mathrm{d}\mathbf{x} = -\int \mathbf{T} : \nabla \boldsymbol{v}\,\mathrm{d}\mathbf{x} - \int_{\partial K} \boldsymbol{v} \cdot \mathbf{T}\mathbf{n}\,\mathrm{d}s\,. \tag{33}$$

The three steps for deriving eq. (24b) are as follows:

*Step 1) Integration over element $K$*

Integrating eq. (2b) over an arbitrary finite element $K$ and applying the integration by parts rules gives,

$$\begin{aligned} -\frac{1}{3}\int_K \nabla \cdot \boldsymbol{v}\,\varphi\,\mathrm{d}\mathbf{x} + \frac{1}{3}\int_{\partial K} \varphi\,(\boldsymbol{v} \cdot \mathbf{n})\,\mathrm{d}s + \int_K \sigma_t\,\boldsymbol{v} \cdot \boldsymbol{J}\,\mathrm{d}\mathbf{x} \\ = \int_K \boldsymbol{v} \cdot \boldsymbol{Q}_1\,\mathrm{d}\mathbf{x} - \int_{\partial K} \boldsymbol{v} \cdot \mathbf{T}\mathbf{n}\,\mathrm{d}s + \int_K \nabla \boldsymbol{v} : \mathbf{T}\,\mathrm{d}\mathbf{x} \quad \forall \boldsymbol{v} \in RT_0\,. \end{aligned} \tag{34}$$

*Step 2) Sum over all elements*

Summing eq. (34) over all elements $K \in \mathcal{T}$ gives,

$$\begin{aligned} -\frac{1}{3}\int \nabla \cdot \boldsymbol{v}\,\varphi\,\mathrm{d}\mathbf{x} + \frac{1}{3}\int_{\partial \mathcal{D}} \varphi\,(\boldsymbol{v} \cdot \mathbf{n})\,\mathrm{d}s + \int \sigma_t\,\boldsymbol{v} \cdot \boldsymbol{J}\,\mathrm{d}\mathbf{x} \\ = \int \boldsymbol{v} \cdot \boldsymbol{Q}_1\,\mathrm{d}\mathbf{x} - \int_{\partial \mathcal{D}} \boldsymbol{v} \cdot \mathbf{T}\mathbf{n}\,\mathrm{d}s - \int_{\Gamma_0} [\![v]\!] \cdot \{\!\{\mathbf{T}\mathbf{n}\}\!\}\,\mathrm{d}s + \int \nabla_h \boldsymbol{v} : \mathbf{T}\,\mathrm{d}\mathbf{x} \quad \forall \boldsymbol{v} \in RT_0\,. \end{aligned} \tag{35}$$

*Step 3) Enforce boundary condition*

"Solving" eq. (2c) for $\varphi$ and substituting the result into the second term in eq. (35) gives the final result, eq. (24b).

An alternative derivation, as well as a hybridized Raviart-Thomas discretization of the second moment system, are provided by Olivier & Haut [22]. The hybridized discretization allows one to solve a smaller system for Lagrange multipliers, after which $\varphi$ and $\boldsymbol{J}$ can be found through element-local back substitution.

Algorithm 2 shows pseudocode for the `second_moment_system_solve()` function in algorithm 1.

**Algorithm 2** Mixed Finite Element Method Solve of Second Moment System

```
function second_moment_system_solve(Q_0, Q_1, T, β)
    A ← assemble_bilinear_form()
    b ← assemble_linear_form(Q_0, Q_1, T, β)
    φ ← linear_solve(A, b)
    return φ
```

*3.3. Discontinuous Finite Element Method for Solving the Transient Heat Conduction Equation*

As indicated in fig. 2, after we solve the second moment system for $\varphi$, we then solve a transient heat conduction equation for $\bar{\varphi}$. We use $\varphi$ as the initial condition and the Dirichlet boundary condition in the standard symmetric interior penalty discontinuous Galerkin (SIPDG) method [25]. For clarity of presentation, we write the Dirichlet boundary data as $\bar{\varphi}_D$ instead of $\varphi$. The SIPDG weak form of eq. (8a) using linear basis functions is: find $\bar{\varphi} \in Y_1$ such that,

$$\frac{\partial}{\partial t}\int u\,\bar{\varphi}\,\mathrm{d}\mathbf{x} + \int \nabla_h u \cdot \frac{1}{\sigma_t}\nabla_h \bar{\varphi}\,\mathrm{d}\mathbf{x} - \int_\Gamma [\![u]\!] \left\{\!\!\left\{ \frac{1}{\sigma_t}\nabla\bar{\varphi}\cdot\mathbf{n} \right\}\!\!\right\} \mathrm{d}s - \int_\Gamma \left\{\!\!\left\{ \frac{1}{\sigma_t}\nabla u\cdot\mathbf{n} \right\}\!\!\right\} [\![\bar{\varphi}]\!]\,\mathrm{d}s$$
$$+ \kappa \int_\Gamma \left\{\!\!\left\{ \frac{1}{h}\frac{1}{\sigma_t} \right\}\!\!\right\} [\![u]\!]\,[\![\bar{\varphi}]\!]\,\mathrm{d}s = -\int_{\Gamma_b} \frac{1}{\sigma_t}\nabla u\cdot\mathbf{n}\,\bar{\varphi}_D\,\mathrm{d}s + \kappa\int_{\Gamma_b}\left\{\!\!\left\{ \frac{1}{h}\frac{1}{\sigma_t} \right\}\!\!\right\} u\,\bar{\varphi}_D\,\mathrm{d}s\,, \quad \forall u \in Y_1\,, \tag{36}$$

where $\Gamma = \Gamma_0 \cup \Gamma_b$ is the set of unique faces in the mesh, $\kappa$ is the penalty parameter, and $h$ is the characteristic mesh element width,

$$h = \max_{K\in\mathcal{T}} \left( \int_{\hat{K}} J\,\mathrm{d}\boldsymbol{\xi} \right)^{1/\dim} . \tag{37}$$

Equation (36) is the standard SIPDG weak form for the model elliptic problem with nonzero Dirichlet boundary conditions, and may be derived following the procedure outlined in Arnold et al. [26].

We discretize time using backward Euler. Let $\Phi$ contain the $Y_1$ degrees of freedom for $\bar{\varphi}$. The ordinary differential equation that arises after assembly of the weak form may be written,

$$M\frac{\mathrm{d}\Phi}{\mathrm{d}t} = -K\Phi + f\,, \tag{38}$$

where $M, K$, and $f$ are the mass matrix, stiffness matrix, and load vector, respectively. Backward Euler is,

$$(M + \Delta t K)\Phi^{n+1} = M\Phi^n + \Delta t\, f\,, \tag{39}$$

where the superscript denotes the timestep index and $\Delta t$ is the timestep size. We compute a single timestep with $\Delta t$ equal to,

$$\Delta t = \alpha h^2 \left( \max_{\mathbf{x}} \sigma_t \right)\,, \tag{40}$$

where we have introduced the timestep control parameter $\alpha \in (0, 1]$ into the timestep size eq. (9) to allow further control of the timestep size.

Algorithm 3 shows pseudocode for the transient heat conduction solve function that is called in algorithm 1. There is no time loop because we only take a single timestep.

## 4. Monte Carlo Component of HSM

We use Monte Carlo to solve the transport equation and compute estimators of the SMM data. Instead of using scattering events, we account for the scattering source by incorporating its contribution into the particle weights. While tracking, we accumulate estimators for the SMM data $\mathbf{T}$ and $\beta$. Specifically, we compute $\hat{\mathbf{T}}$, which is an estimator for $\mathbf{T}$, using path length estimators in each element. Let $\mathrm{vol}(K)$ be the

**Algorithm 3** Discontinuous Finite Element Method Solve of Transient Heat Conduction Equation

```
function transient_heat_conduction_solve(φ)
    A ← assemble_bilinear_form()
    b ← assemble_linear_form(φ)
    φ̄ ← linear_solve(A, b)
    return φ̄
```

volume of element $K$, $d$ the length of a path traversed by a particle in $K$, and $w$ the weight of the particle that traversed the path. Then,

$$\hat{\mathbf{T}} = \hat{\mathbf{P}} - \frac{1}{3}\mathbf{I}\hat{\phi}\,, \tag{41a}$$

$$\hat{\phi} = \frac{1}{\text{vol}(K)} \sum_i d_i w_i\,, \tag{41b}$$

$$\hat{\mathbf{P}} = \frac{1}{\text{vol}(K)} \sum_i \boldsymbol{\Omega}_i \otimes \boldsymbol{\Omega}_i \, d_i w_i\,, \tag{41c}$$

where the index $i$ is associated with a particle path, so $\boldsymbol{\Omega}_i$ is the (entire) direction vector of the particle that traversed path $i$ (*not* the $i$th component of the direction vector). Equations (41b) and (41c) are path length estimators for the zeroth and second angular moments of the intensity, respectively.

We compute $\hat{\beta}$, which is an estimator for $\beta$, using surface crossing estimators on each boundary face. Let area($\mathcal{F}$) be the area of boundary face $\mathcal{F}$. Then,

$$\hat{\beta} = \hat{B} - \frac{1}{2}\hat{\phi}_s\,, \tag{42a}$$

$$\hat{B} = \frac{2}{\text{area}(\mathcal{F})} \sum_i w_i\,, \tag{42b}$$

$$\hat{\phi}_s = \frac{2}{\text{area}(\mathcal{F})} \sum_i \frac{w_i}{|\boldsymbol{\Omega}_i \cdot \mathbf{n}|}\,, \tag{42c}$$

Equations (42b) and (42c) are surface crossing estimators for the first and zeroth angular moments of the intensity on a surface, respectively. Derivations of eqs. (41b), (41c), (42b) and (42c) can be found in Chapter 3 of Pozulp [27].

Every source is either a volume source in some subset of the domain, or a surface source on some subset of the domain boundary. Below, we describe how we compute weights for volume source particles and for boundary source particles. Consider the arbitrary source function $q = q(\mathbf{x}, \boldsymbol{\Omega})$, which is a volume source. Let $U(\cdot)$ be a uniformly-distributed random variate on some domain. For example, $U(a, b)$ is uniform on $(a, b)$. The weights that we assign to the particles sourced from the volume source $q$ are,

$$w_i = \frac{4\pi \,\text{vol}(\mathcal{D})}{N}\, q(\boldsymbol{x}_i, \boldsymbol{\Omega}_i)\,, \qquad \boldsymbol{x}_i \leftarrow U(\mathcal{D})\,, \qquad \boldsymbol{\Omega}_i \leftarrow U(\mathbb{S}^2) \tag{43}$$

where $N$ is the number of particles sourced from $q$ and $\leftarrow$ denotes the generation of a random variate. The weights that we assign to the particles sourced from the inflow boundary source $\psi_{\text{inc}}(\mathbf{x}, \boldsymbol{\Omega})$ are,

$$w_i = \frac{2\pi \,\text{area}(\partial\mathcal{D})}{M} |\boldsymbol{\Omega}_i \cdot \mathbf{n}| \psi_{\text{inc}}(\boldsymbol{x}_i, \boldsymbol{\Omega}_i)\,, \qquad \boldsymbol{x}_i \leftarrow U(\partial\mathcal{D})\,, \qquad \boldsymbol{\Omega}_i \leftarrow U(\mathbb{S}^2_h) \tag{44}$$

where $M$ is the number of particles sourced from $\psi_{\text{inc}}$, and $\mathbb{S}^2_h$ is the unit hemisphere at $\boldsymbol{x}_i$ defined by $\boldsymbol{\Omega}_i \cdot \mathbf{n} < 0$. Algorithm 4 shows pseudocode for the Monte Carlo transport solve function that is called in algorithm 1. There are no scattering events; the contribution of the scattering source is included in the particle weights.

**Algorithm 4** Monte Carlo Solve of Linear Transport Equation

```
function mc_transport_solve(vs, bs)
    particles ← sample_volume_source(vs)
    particles ← particles + sample_boundary_source(bs)
    tallies ← 0
    while any(particles.alive) do
        intersection_distances ← compute_distances(particles)
        collision_distances ← sample_distances(particles)
        intersection_mask ← intersection_distances < collision_distances
        collision_mask ← intersection_distances > collision_distances
        tallies ← tallies + move_across_element_boundary(particles[intersection_mask])
        tallies ← tallies + move_to_collision_location(particles[collision_mask])
        particles[collision_mask].alive ← false
    return tallies
```

*4.1. Thick Diffusion Limit Analysis*

In section 1, we mentioned that a Monte Carlo estimator of the solution to eq. (6) would have a variance that approaches infinity in the thick diffusion limit (TDL). Here, we define the dependence of the variance on the TDL parameter $\epsilon$, the order of the total source function $Q$, and the order of the inflow source function $\psi_{\text{inc}}$. The function $Q$ is simply the right-hand side of the transport equation. The value of $Q$ for eq. (6) is the product of the scattering source and the inhomogeneous source function,

$$Q = \frac{\sigma_s}{4\pi}\varphi + q\,. \tag{45}$$

The connection between the variance of our MC estimators, $\epsilon, \psi_{\text{inc}}$, and $Q$ is stated in theorem 1.

**Theorem 1.** *Let $Q$ be the total source function of a transport problem with the following form,*

$$\boldsymbol{\Omega}\cdot\nabla\psi + \sigma_t\psi = Q\,,$$

*subject to the inflow boundary condition,*

$$\psi(\mathbf{x},\boldsymbol{\Omega}) = \psi_{inc}(\mathbf{x},\boldsymbol{\Omega})\,, \quad \mathbf{x}\in\partial\mathcal{D} \text{ and } \boldsymbol{\Omega}\cdot\mathbf{n} < 0\,.$$

*Let* $\text{Var}[\cdot]$ *be the variance of an estimator for some quantity in a weighted Monte Carlo particle simulation of this transport problem, such as the angle integrated intensity, and let $\epsilon$ be the thick diffusion scaling limit (TDL) parameter. Then* $\text{Var}[\cdot]$ *is,*

$$O\left(\max\left\{\text{order}(Q)^2, \text{order}(\psi_{inc})^2\right\}\epsilon\right),$$

*where* $\text{order}(Q)$ *and* $\text{order}(\psi_{inc})$ *are the powers of $\epsilon$ which define the leading order term in the TDL scaling of $Q$ and $\psi_{inc}$, respectively.*

A proof is provided in Pozulp and Haut [28].

Theorem 1 is the motivation for the transient heat conduction solve in HSM. We show this by using theorem 1 to derive the dependence of the variance of our estimators on $\epsilon$ for different $Q$. First, we assume that $\psi_{\text{inc}}$ is $O(1)$, which simplifies the variance expression in theorem 1 to $O(\max\{\text{order}(Q)^2, 1\}\,\epsilon)$. Impose the TDL scaling of the transport equation data [3],

$$\sigma_t \leftarrow \sigma_t/\epsilon\,, \tag{46a}$$

$$\sigma_a \leftarrow \sigma_a\epsilon\,, \tag{46b}$$

$$q \leftarrow q\epsilon\,. \tag{46c}$$

Thus, $\sigma_a$ and $q$ are $O(\epsilon)$, $\sigma_t$ and $\sigma_s$ are $O(1/\epsilon)$ because $\sigma_s = \sigma_t - \sigma_a$, and $\varphi$ is $O(1)$. We can label the terms and coefficients in the total source function from the untransformed transport eq. (6) to determine how $Q$ scales with $\epsilon$ as follows,

$$Q = \underbrace{\frac{\sigma_s}{4\pi}\varphi}_{O(\epsilon^{-1})} + \underbrace{q}_{O(\epsilon)}\,. \tag{47}$$

Thus, $Q$ for eq. (6) is $O(1/\epsilon)$, because $1/\epsilon \gg \epsilon$. By theorem 1, Var[·] is $O(1/\epsilon)$ for estimators computed in a weighted Monte Carlo particle simulation of the untransformed problem. The variance limits to infinity. The MC solution of the untransformed problem is infinitely noisy in the TDL.

Now consider the total source function in the transformed problem, defined by eqs. (7a) and (7b), which introduces the arbitrary function $\bar{\varphi}$. Recall from the HSM algorithm description in section 2 that we choose $\bar{\varphi}$ such that $\varphi - \bar{\varphi}$ is $O(1/\sigma_t)$. The reason that we make this choice is to preserve the order reduction of $O(1/\epsilon)$ to $O(1)$ for $Q$ that is achieved when $\bar{\varphi} = \varphi$. As previously noted, we do not use $\bar{\varphi} = \varphi$ because we want to avoid material interface sources and well-posedness concerns. We want $\varphi - \bar{\varphi}$ to be $O(1/\sigma_t)$ because of how the terms in the $Q$ for eq. (7a) scale,

$$Q = \frac{\sigma_t}{4\pi}(\varphi - \bar{\varphi}) - \underbrace{\frac{1}{4\pi}(\underbrace{\sigma_a\varphi}_{O(\epsilon)} + \underbrace{\mathbf{\Omega}\cdot\nabla\bar{\varphi}}_{O(1)})}_{O(1)} + \underbrace{q}_{O(\epsilon)}\,. \tag{48}$$

Thus, $Q$ for eq. (7a) scales as,

$$O\Big(\max\Big\{\text{order}\Big(\frac{\sigma_t}{4\pi}(\varphi - \bar{\varphi})\Big),\, 1\Big\}\Big)\,. \tag{49}$$

We seek an order reduction of $O(1/\epsilon)$ to $O(1)$ for $Q$. We achieve this by choosing $\bar{\varphi}$ such that $\varphi - \bar{\varphi}$ is $O(1/\sigma_t)$. By theorem 1, Var[·] is $O(\epsilon)$ for estimators computed in a weighted Monte Carlo particle simulation of the transformed problem. The variance limits to zero. Thus, the variance of estimators for the transformed problem is substantially lower because it limits to zero instead of infinity in the TDL. This result is what gives HSM the desirable property of requiring fewer MC particles to achieve a desired uncertainty as the optical thickness of the transport problem increases.

## 5. Numerical Results

We implemented an MPI-parallel Monte Carlo solver in the C programming language which distributes the simulation particles evenly amongst the MPI ranks. All ranks source and track particles. To implement the second moment system and the transient heat conduction equation solvers, we used the C++ programming language with the MPI-parallel finite element library MFEM [29] along with the MPI-parallel sparse iterative linear solvers library HYPRE [30] and the MPI-parallel sparse direct linear solver library SuperLU [31]. We used HYPRE's algebraic multigrid preconditioner with the conjugate gradient solver to invert the coefficient matrix in the discretized transient heat conduction system defined by eq. (39). We used SuperLU to invert a Schur complement of one of the diagonal blocks of the second moment system block operator after computing the inverse of another block of element matrices using element-wise Gauss-Jordan elimination with partial pivoting. We used SuperLU because, in the largest problem we considered, inverting the second moment system accounted for less than 4% of the total calculation runtime. This allowed us the luxury of computing the solution to (a small multiple of) machine precision. However, SuperLU is not required; fast iterative linear solvers can be used to invert the second moment system and have been shown to be efficient on large second moment systems for various polynomial orders, as demonstrated by Olivier & Haut [22]. We set the penalty parameter to $\kappa = 4$ and the timestep control parameter to $\alpha = 0.001$. We source the same number of particles in the domain and on its boundary, so $N = M$ in eqs. (43) and (44).

We present numerical results for different linear transport problems modeled by eq. (1a) with the boundary condition eq. (1b). In section 5.1, we solve a problem with a single material to verify that our HSM

method has a numerical error that agrees with our expectation for how the error should depend on the number of particles and the element width. In section 5.2, we solve another single-material problem, the purpose of which is to show how the HSM solution behaves as the optical thickness of the material increases. Finally, in section 5.3, we solve a proxy problem from radiative transfer that contains both optically-thick and optically-thin material, and show that our hybrid method runs orders of magnitude faster than Monte Carlo, without sacrificing accuracy. Our numerical results provide what we believe to be the first demonstration of a hybrid SMM in more than one spatial dimension, the first to consider more than one material, and the first to use variance reduction.

*5.1. Method of Manufactured Solutions Problem*

The Method of Manufactured Solutions (MMS) is a code verification technique in which one chooses an analytic solution, which is called the "MMS solution". One then substitutes the MMS solution into the partial differential equation to derive expressions for the problem data, which includes: sources, boundary conditions, and the initial condition [32, 33, 34]. We use MMS to verify that our HSM method has a numerical error of $O(h)+O(N^{-1/2})$, where $h$ is the characteristic mesh length defined by eq. (37), and $N$ is the number of MC particles. The first term is due to the $h^{p+1}$ convergence of the mixed finite element discretization of the second moment system, where $p = 0$ in our case because we use $Y_1$, $RT_0$, and piecewise constant MC estimators for the SMM data. The second term is due to the $\sqrt{\text{Var}[\cdot]/N}$ uncertainty of the estimators computed in the Monte Carlo component of HSM. The hypothesized convergence rate of $O(h) + O(N^{-1/2})$ defines an error surface that decreases in height as one traverses simultaneously upward and rightward in fig. 5.

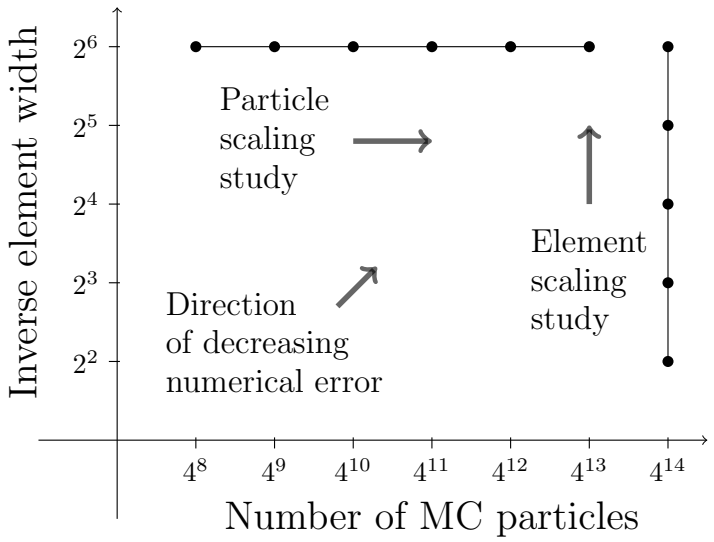


Figure 5: Calculation points on the HSM error surface.

By making $h$ small and running multiple calculations with increasing $N$ in the "particle scaling study", we observe the $O(N^{-1/2})$ term in the hypothesized convergence rate, and by making $N$ large and running multiple calculations with decreasing $h$ in the "element scaling study", we observe the $O(h)$ term. We let $\mathcal{D} = [0, 1]^2$, $\sigma_t = 2$, $\sigma_s = 1$, and we solve the problem specified by eqs. (1a) and (1b) for the MMS solution in Equation (89) in [35]. The MMS solution is,

$$\psi_{\text{MMS}}(\mathbf{x}, \mathbf{\Omega}) = \frac{1}{4\pi}\Big( \sin(\pi x)\sin(\pi y) + \mathbf{\Omega}_x \mathbf{\Omega}_y \sin(2\pi x)\sin(2\pi y) + \mathbf{\Omega}_x^2 \sin\Big(\frac{5\pi}{2}x + \frac{\pi}{4}\Big)\sin\Big(\frac{5\pi}{2}y + \frac{\pi}{4}\Big) + 0.5\Big). \quad (50)$$

We substitute the MMS solution into the equations on the left of fig. 1, solve for $q$ and $\psi_{\text{inc}}$, and use them in the MC component of our HSM solver. Similarly, we substitute the MMS solution into the equations on the right of fig. 1, solve for $Q_0$, $\boldsymbol{Q}_1$, and $J_{\text{in}}$, and use them in the deterministic component of our HSM solver. The MMS source expressions for $q, \psi_{\text{inc}}, Q_0, \boldsymbol{Q}_1$ and $J_{\text{in}}$ can be found in Section 5.1.1 of [27].

Equation (50) cannot be computed with the radiation diffusion approximation because it is quadratically-anisotropic. Additionally, eq. (50) exercises the coupling of the MC component of HSM with the deterministic component of HSM because it has nonzero SMM data $\mathbf{T} \neq 0$ and $\beta \neq 0$. Finally, eq. (50) also exercises our implementation of the boundary conditions because it has nonzero inflow $\psi_{\text{inc}} \neq 0$, and so $J_{\text{in}} \neq 0$.

The solution that we seek with HSM is the angle integrated intensity, which we can express analytically by integrating eq. (50) over the unit sphere to get,

$$\phi_{\text{MMS}}(\mathbf{x}) = \sin(\pi x)\sin(\pi y) + \frac{1}{3}\sin\left(\frac{5\pi}{2}x + \frac{\pi}{4}\right)\sin\left(\frac{5\pi}{2}y + \frac{\pi}{4}\right) + 0.5\,. \tag{51}$$

The HSM estimator approximates the average angle integrated intensity on each element. Averaging eq. (51) over an arbitrary rectangle gives the analytic expression to which we compare our HSM solution,

$$\bar{\phi}_{\text{MMS}}(x_1, x_2, y_1, y_2) = \frac{1}{(x_2 - x_1)(y_2 - y_1)} \int_{x_1}^{x_2} \int_{y_1}^{y_2} \phi_{\text{MMS}}(\mathbf{x})\,\mathrm{d}y\,\mathrm{d}x\,. \tag{52}$$

Evaluating the integrals in eq. (52) gives the final analytic expression,

$$\begin{aligned}\bar{\phi}_{\text{MMS}}(x_1, x_2, y_1, y_2) = \frac{1}{(x_2 - x_1)(y_2 - y_1)} \Bigg( & \frac{1}{\pi^2}\left\{\Big[\cos(\pi x_2) - \cos(\pi x_1)\Big]\Big[\cos(\pi y_2) - \cos(\pi y_1)\Big]\right\} \\ & + \frac{4}{75\pi^2}\left\{\left[\cos\left(\frac{5\pi}{2}x_2 + \frac{\pi}{4}\right) - \cos\left(\frac{5\pi}{2}x_1 + \frac{\pi}{4}\right)\right]\left[\cos\left(\frac{5\pi}{2}y_2 + \frac{\pi}{4}\right) - \cos\left(\frac{5\pi}{2}y_1 + \frac{\pi}{4}\right)\right]\right\}\Bigg)\,.\end{aligned} \tag{53}$$

We use a computational mesh of equally-sized squares, so we simply evaluate eq. (53) using the $x_1, x_2, y_1$, and $y_2$ values which define the left, right, bottom, and top edges of each square in our mesh. Figure 6 shows plots of $\phi_{\text{MMS}}$ and $\bar{\phi}_{\text{MMS}}$ on the calculation domain $\mathcal{D} = [0, 1]^2$.

We determine the error of our numerical solution with respect to eq. (53) in the element scaling study by computing the norm of the difference and dividing by the square root of the number of elements,

$$\text{Element scaling study error} = h||\hat{\phi} - \bar{\phi}_{\text{MMS}}||_2\,, \tag{54}$$

where $h$ is the characteristic mesh length defined by eq. (37). In the particle scaling study, the mesh is fixed at $64 \times 64$ elements for all 6 calculations, so the normalization factor $h$ in eq. (54) is replaced by unity,

$$\text{Particle scaling study error} = ||\hat{\phi} - \bar{\phi}_{\text{MMS}}||_2\,. \tag{55}$$

Derivations of eqs. (54) and (55) may be found in Section 5.1 of [27].

The results in fig. 7 demonstrate that HSM converges under mesh refinement and MC sample augmentation, and that the rate of convergence with respect to the element width and number of MC particles matches our hypothesis of $O(h) + O(N^{-1/2})$. The slight degradation in convergence at the highest mesh resolution, appearing as liftoff above the dashed curve at the bottom-left of fig. 7b, is expected behavior because we distribute a fixed number of MC particles across more and more elements under mesh refinement. We confirmed that this was the case by running fewer MC particles and observing earlier liftoff, as well as running more MC particles and observing delayed liftoff.

### *5.2. Thick Diffusion Limit Problems*

The thick diffusion limit, characterized by the parameter $\epsilon \in (0, 1]$ when $\epsilon \to 0$ for the problem data scalings defined in eqs. (46a) to (46c), is a challenging regime for transport methods. Unaccelerated source

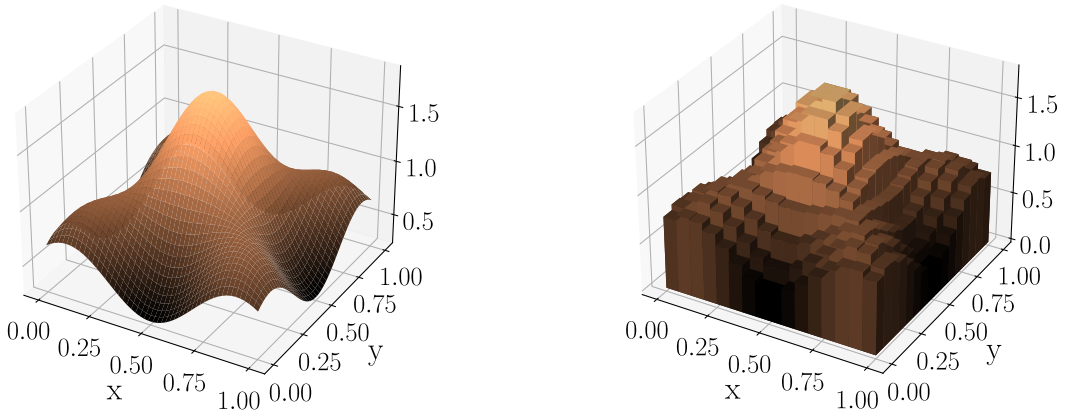


(a) $\phi_{\text{MMS}}(\mathbf{x})$

(b) $\bar{\phi}_{\text{MMS}}(x_1, x_2, y_1, y_2)$

Figure 6: The MMS solution eq. (51) and its average eq. (53) on $\mathcal{D} = [0,1]^2$.

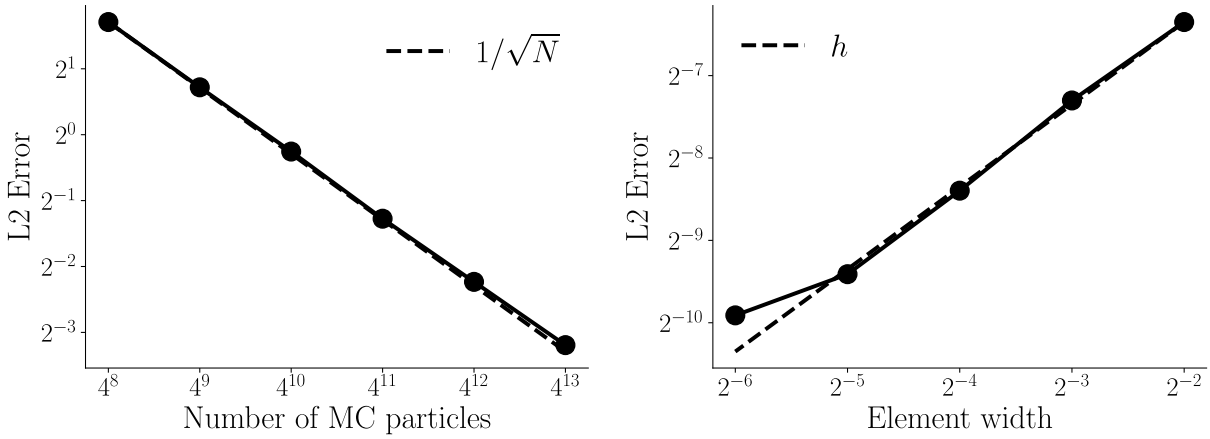


(a) Error as number of MC particles increases.

(b) Error as element width decreases.

Figure 7: Error of HSM iterate $\hat{\phi}^{(i)}$ upon convergence.

iteration calculations require $O(1/\epsilon^2)$ iterations to converge, and unaccelerated MC calculations require $O(1/\epsilon^2)$ runtime to finish. We show that the HSM runtime is independent of $\epsilon$, and that our variance reduction provides the desirable $O(\epsilon)$ estimator variance, rather than $O(1/\epsilon)$.

Let $\mathcal{D} = [0,1]^2$ as in section 5.1, but now define the problem data in eqs. (1a) and (1b) using the TDL scaling eqs. (46a) to (46c). Thus, unlike in our MMS calculation where $\sigma_t = 2$ and $\sigma_s = 1$, here we use $\sigma_t = 1/\epsilon$ and $\sigma_s = 1/\epsilon - \epsilon$. Also, in our MMS calculation, $q$ is a complicated expression derived by substituting the MMS solution into eq. (1a). Here, we use the very simple expression $q = \epsilon$.

Consider four different $\epsilon$ values: $10^{-1}, 10^{-2}, 10^{-3}$, and $10^{-4}$. We run calculations for each value using 10 million HSM volume source particles, no boundary source particles, and a vacuum boundary condition. We compute the angle integrated intensity averaged over each element in an 8-by-8 mesh of squares of equal size. Our solution is a surface on the $xy$-plane. We present HSM solution lineouts. Figure 8 shows that our HSM solution appears to converge to the diffusion limit solution as $\epsilon \to 0$ because the lineouts appear to approach an equilibrium solution in the sense that successive lineouts differ less for smaller $\epsilon$.

What about runtime? The convergence depicted by fig. 8, which shows solution lineouts for four calcula-

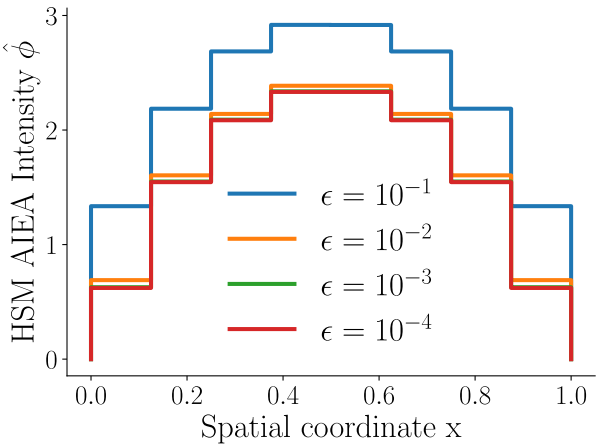


Figure 8: Lineouts at $y = 0.5$ of HSM angle integrated element averaged (AIEA) intensity for calculations using four different values of the TDL scaling parameter $\epsilon$.

tions using the HSM method, would be the same picture for unaccelerated Monte Carlo (UMC)[1]. However, the runtimes of HSM and UMC in the TDL are very different. Figure 9 shows that the HSM runtime is constant with respect to the TDL scaling parameter, or $O(1)$, whereas the UMC runtime increases quadratically with the inverse of $\epsilon$, or $O(1/\epsilon^2)$. HSM substantially outperforms UMC in terms of runtime as $\epsilon \to 0$.

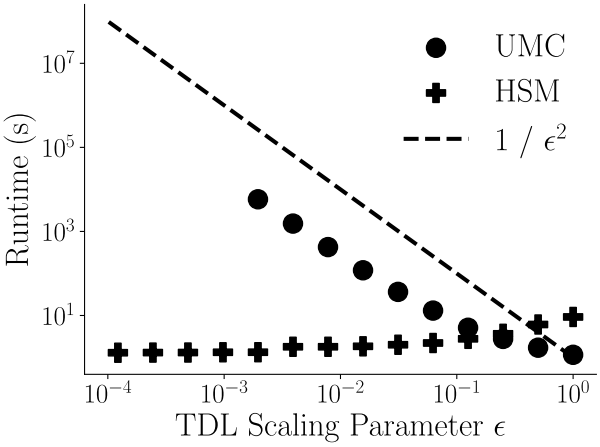


Figure 9: Runtime of unaccelerated Monte Carlo (UMC) and hybrid second moment (HSM) methods for calculations with different values of the TDL scaling parameter $\epsilon$. The $\epsilon$ values are $2^0, 2^{-1}, 2^{-2}, \ldots, 2^{-13}$.

What about variance? A common figure of merit used with MC methods is the inverse of the product of the variance and the runtime,

$$\text{Figure of merit} = \frac{1}{\text{Var}[\cdot]\, T}\,, \tag{56}$$

where Var$[\cdot]$ is the variance of some estimator and $T$ is the runtime of the calculation. Decreasing either Var$[\cdot]$ or $T$ increases the figure of merit. Reading fig. 9 from right to left, we observe that $T_{\text{HSM}} < T_{\text{UMC}}$

[1]We use the acronym UMC (instead of MC) to emphasize that the solution we compare with our HSM approach does not employ any of the acceleration techniques described in section 1, such as Fleck & Canfield's Random Walk, IMD, or DDMC.

after $\epsilon$ falls below a value somewhere between $\epsilon = 1/4$ and $1/8$, and that $T_{\text{HSM}} << T_{\text{UMC}}$ beginning at about $\epsilon = 1/32$, which is a result that holds for all smaller $\epsilon$ values. This factor of $\epsilon^2$ decrease in the runtime would be useless if the variance of the HSM estimator increased by a factor of $1/\epsilon^2$ relative to the UMC variance, because eq. (56) shows that the figure of merit would be left unchanged.

We calculate the variance of the HSM solution in the TDL by running 600 realizations of the same calculation on a single-element mesh with a different pseudo-random number generator seed for each calculation. Each calculation computes the angle integrated intensity averaged over the lone mesh element. The domain is $\mathcal{D} = [0, 1]^2$. We use 100 million HSM particles for each calculation. We consider five different optical thickness parameter values, $10^{-1}, 10^{-2}, 10^{-3}, 10^{-4}$, and $10^{-5}$. Thus, the total number of calculations is $600 \times 5 = 3000$. We estimate the variance as the sum of squares of the difference of the HSM angle integrated element averaged intensity estimator realizations with the mean estimate,

$$\text{Var}[\hat{\phi}] \approx \frac{1}{600} \sum_{i=1}^{600} (\hat{\phi}_i - \Phi)^2 \,, \tag{57}$$

where $\Phi$ is the mean estimate defined by $\Phi = (1/600) \sum_{i=1}^{600} \hat{\phi}_i$. Figure 10 shows that the empirical variance of the HSM estimator $\hat{\phi}$ in the TDL before variance reduction is $O(1/\epsilon)$, which matches our expectation based on the fact that $\text{Var}[\hat{\phi}]$ is $O(1/\epsilon)$ when $Q$ is $O(1/\epsilon)$, and after variance reduction is $O(\epsilon)$, which matches our expectation based on the fact that $\text{Var}[\hat{\phi}]$ is $O(\epsilon)$ when $Q$ is $O(1)$.

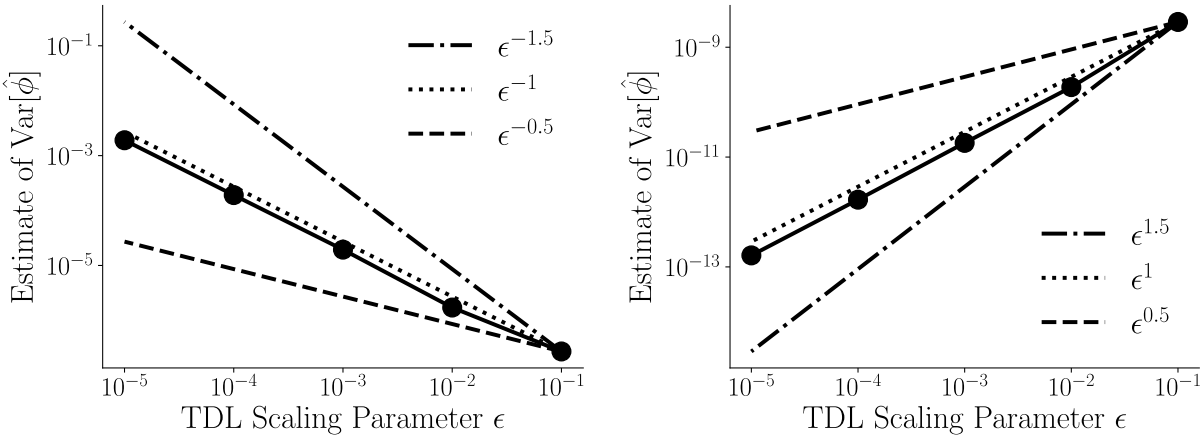


(a) Variance of HSM estimator for eq. (6).

(b) Variance of HSM estimator for eq. (7a).

Figure 10: Hybrid Second Moment estimator variance before variance reduction (a) and after variance reduction (b).

### *5.3. Linearized Crooked Pipe Problem*

We now consider a problem containing both optically-thick and optically-thin material. The Crooked Pipe is a thermal radiative transfer benchmark problem proposed by Graziani and LeBlanc [36]. The authors describe radiation flow down a pipe with a bend. In the Crooked Pipe problem description, a boundary source of radiation shines on one end of an optically-thin pipe surrounded by an optically-thick medium. Radiation flows preferentially through the pipe, around a bend in the pipe, and then leaves the problem through a vacuum boundary on the other end of the pipe.

Crooked Pipe is a time-dependent problem. The solution described in the problem statement is the temperature time-series at five fiducial points inside the pipe. We solve a steady-state simplification sometimes called the Linearized Crooked Pipe. The linearization is equivalent to calculating one very large timestep of a backward Euler time integrator. The timestep is such that $c\Delta t = 10^3$. The pipe is 1000 times optically thinner than the surrounding medium. Figure 11 depicts the geometry, material data, and boundary

conditions for the problem. The boundary source is isotropic on the inflow hemisphere with magnitude,

$$\psi_{\text{inc}} = \begin{cases} \frac{1}{2\pi} & x = 0 \text{ and } -0.5 < y < 0.5\,, \\ 0 & \text{otherwise}\,. \end{cases} \tag{58}$$

Finally, there is an isotropic volume source with constant value $q = 10^{-7}$ everywhere in space, which emulates the material emission source term in the thermal radiative transfer equations.

Consider a mesh composed of squares of equal sizes. The minimal number of uniform squares required to tessellate the geometry such that all material interfaces are on element boundaries is $14 \times 8 = 112$. Figure 12a shows the aforementioned mesh elements, all of which contain material with single-valued properties, because each element contains either optically-thin pipe material, or optically-thick surrounding material, but not both. Figure 12b shows the mesh after splitting each element into four squares of equal size to create a new mesh with 28 × 16 elements. Repeating this refinement operation three more times results in a 224 × 128 mesh, with 28,672 square elements, which is the mesh that we used in our calculations. We set the convergence threshold $\eta$ in the convergence criterion eq. (11) to $10^{-3}$. We computed a piecewise constant angle integrated intensity using our $\hat{\phi}$ estimator of $\phi$. Our estimator approximates the average of $\phi$ on each element, meaning that it is single-valued within a mesh element.

We ran three calculations. We computed HSM and UMC solutions using 16 million simulation particles. We also computed a radiation diffusion approximation solution. Figure 13 shows pseudocolor plots of the three solutions. Three comments regarding the results in fig. 13 are:

1. The HSM and UMC solutions agree to about 3% in the infinity norm ($1.82/1.76 \approx 1.03$).

2. The bright illumination of the front wall and the dark shadowing of the back wall are the most prominent in UMC, remain visible in HSM, and are nearly indiscernible in the diffusion approximation.

3. Similarly, the section of pipe nearest to the right boundary is darkest in UMC and brightest in the diffusion approximation, with HSM somewhere in between.

Without variance reduction, HSM requires about 500 times more simulation particles—8 billion instead of 16 million—to provide a solution with as little noise as UMC. While we do not present the noisy solution here, it can be found in the final figure of [28], which includes a pseudocolor plot of the noisy solution.

What about runtime? We ran the HSM and UMC calculations with 500 and 100 different pseudo-random number seeds, respectively, and found that the median runtime was about two orders of magnitude faster for HSM (which is why we ran five times more HSM calculations). The substantial runtime savings is due to the cost of the billions of scattering events in the UMC calculation, which we completely avoid by not having scattering events in the HSM algorithm.

What about variance? When calculating the variance for the collection of 500 HSM calculations and 100 UMC calculations, we get one value per mesh element. We desire a transport method with high global accuracy, so we choose to compare the maximum of the element variances. We found that the maximum variance is about one order of magnitude lower for UMC than for HSM. Thus, the figure of merit defined by eq. (56) is about one order of magnitude greater for HSM than UMC. Table 1 summarizes these results.

Figure 14 shows pseudocolor plots of the variance, revealing that the UMC variance is highest in the optically-thick material, while the HSM variance peaks at the inflow boundary. This suggests that we could reduce the HSM variance by sourcing more particles in the elements near the inflow boundary during the HSM iteration. In general, it would be better to sample the variable sources non-uniformly. This approach would provide a particle weight distribution with reduced dispersion, thereby decreasing the HSM variance.

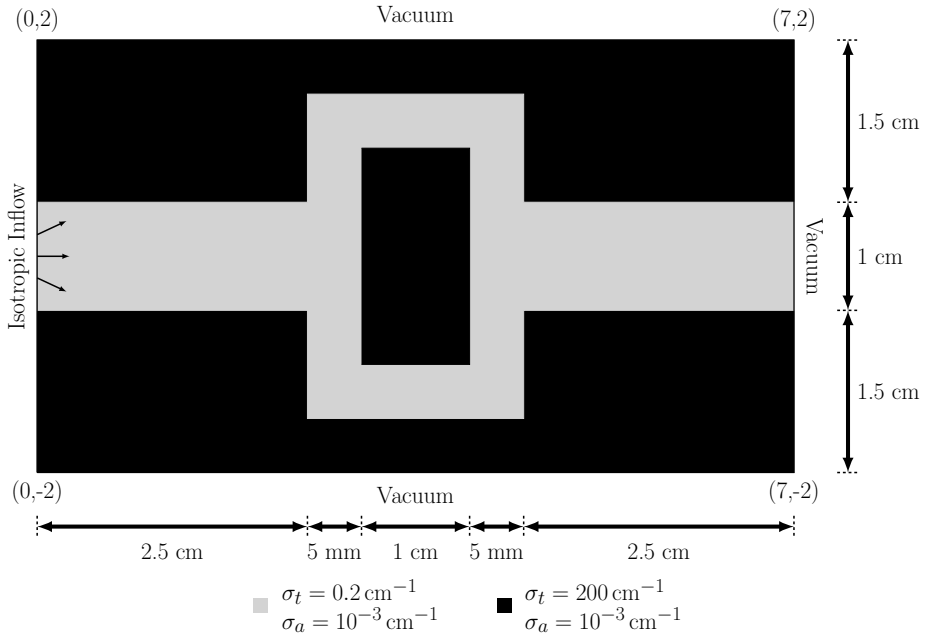


Figure 11: Linearized Crooked Pipe geometry, material data, and boundary conditions [35].

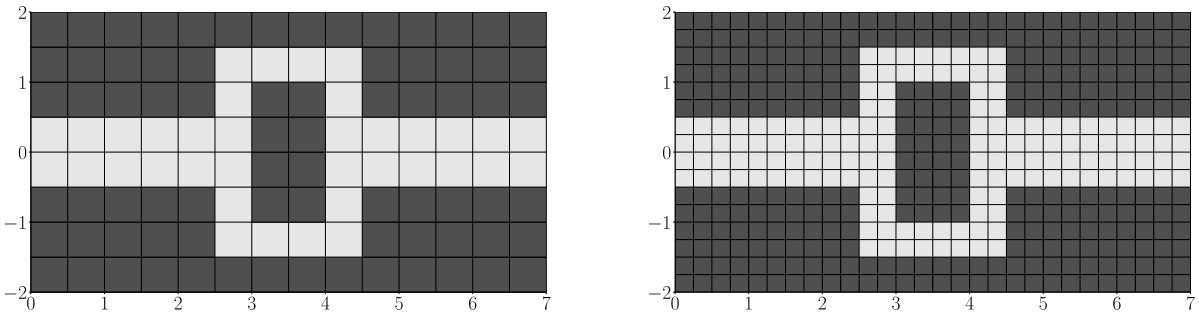

(a) $|\mathcal{T}| = 14 \times 8 = 112$ elements.

(b) $|\mathcal{T}| = 28 \times 16 = 448$ elements.

Figure 12: Minimal uniform square mesh of the Linearized Crooked Pipe geometry with single-valued material property elements (a), and the same mesh after splitting each element into four squares of equal size (b).

| | Runtime | Variance | FOM |
|---|---|---|---|
| HSM | 0m 22s | $3.66 \cdot 10^{-4}$ | 124.2 |
| UMC | 41m 35s | $5.20 \cdot 10^{-5}$ | 7.7 |

Table 1: Median runtime, maximum variance, and figure of merit (FOM) for HSM and UMC calculations using 500 and 100 different pseudo-random number seeds, respectively.

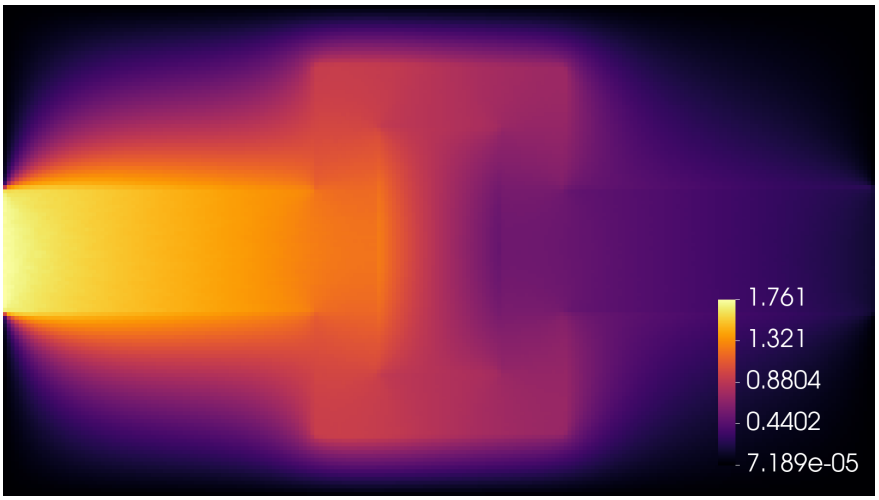


(a)

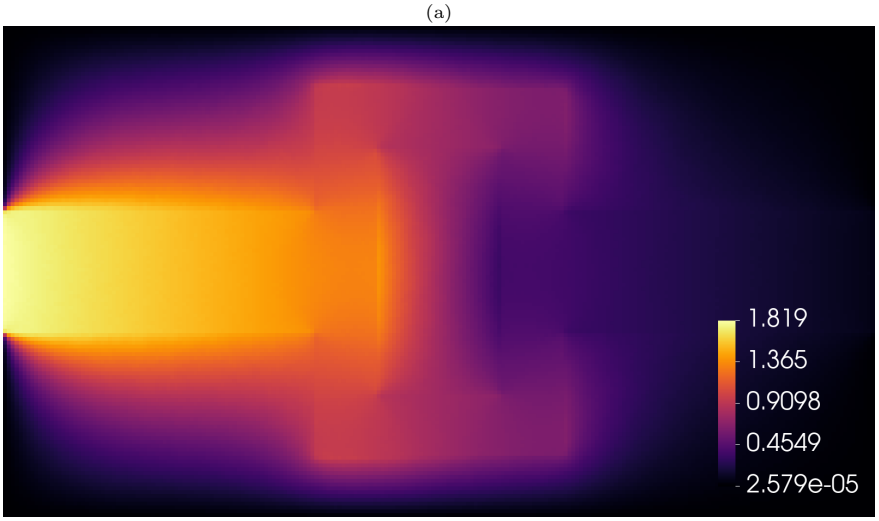


(b)

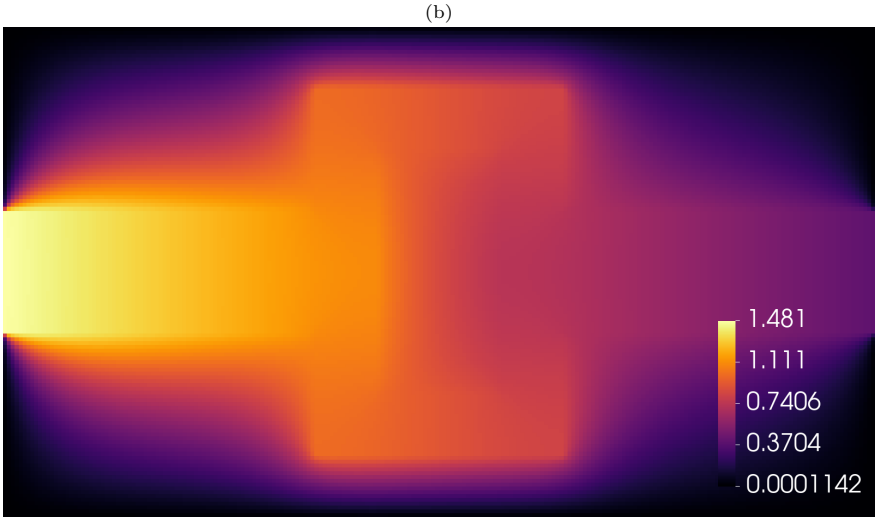


(c)

Figure 13: HSM (a), UMC (b), and diffusion (c) solutions for the Linearized Crooked Pipe.

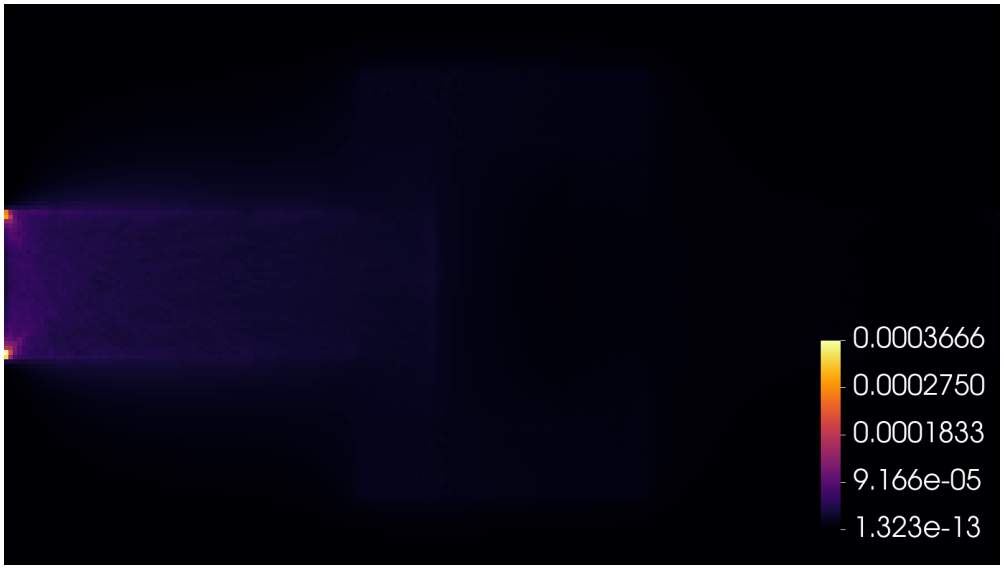


(a)

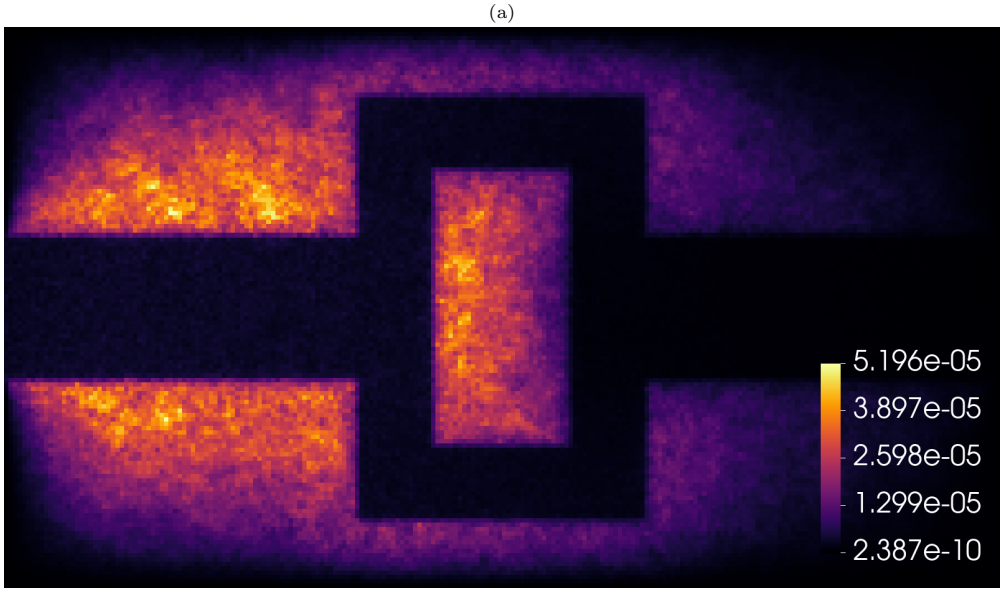


(b)

Figure 14: The variance of the solution estimator for HSM (a) and UMC (b).

## 6. Conclusions

In this work, we presented what we believe to be the first demonstration of a hybrid Second Moment Method for linear transport in more than one spatial dimension, the first to consider more than one material, and the first to use variance reduction. We refer to our method as hybrid Second Moment (HSM).

HSM uses Monte Carlo (MC) instead of $S_N$ to invert the transport operator. This approach avoids unphysical starburst patterns in the numerical solution, known as "ray effects", which are caused by angular under-resolution in $S_N$ methods. However, using MC introduces a variance issue, which we addressed by computing the deviation of the radiation intensity from isotropy. The magnitude of the source in the transformed problem is bounded, and the quality of the hybrid method solution is dramatically improved by a substantial reduction in the variance. Our analysis of the thick diffusion limit (TDL) provided a theoretical basis for the variance that we should expect with HSM, and we included a numerical demonstration of the hypothesized value. This motivated the inclusion of a transient heat conduction solve which, along with the second moment system solve, forms the deterministic component of HSM.

We showed that HSM performs well on a proxy problem from radiative transfer containing both optically-thick and optically-thin material. In this way, HSM is similar to thermal radiative transfer algorithms such as IMD or DDMC, which dramatically reduce the expense of implicit Monte Carlo (IMC) calculations in the TDL. However, IMD and DDMC make diffusion approximations, require phase-space partitioning, and have yet to be extended to reentrant elements. HSM does not make a diffusion approximation, does not partition phase-space, and does not require a non-reentrant mesh. Table 2 summarizes these differences.

Future work on HSM could include investigating alternatives to the transient heat conduction solve, improvements to reduce the variance in the Linearized Crooked Pipe problem relative to unaccelerated Monte Carlo, comparisons in cost/accuracy to IMD and DDMC, extending HSM to TRT, and accommodating more physics such as line transport or Compton scattering in the MC solve and the deterministic low-order system.

| | HSM | IMD or DDMC |
|---|---|---|
| Orders of magnitude speedups | ✓ | ✓ |
| No diffusion approximation | ✓ | × |
| No phase-space partitioning | ✓ | × |
| No issues with reentrant elements | ✓ | × |
| No iteration | × | ✓ |
| No linear solver | × | ✓ |
| No negative energy-weight | × | ✓ |
| Demonstrated in production calculations | × | ✓ |

Table 2: Comparison of HSM and IMD or DDMC for selected qualities.

## 7. Acknowledgements

This work was performed under the auspices of the U.S. Department of Energy by Lawrence Livermore National Laboratory under Contract DE-AC52-07NA27344. LLNL-JRNL-2010906-DRAFT.

## References

[1] E. Lewis and W. Miller, "A comparison of p1 synthetic acceleration techniques," *Transactions of the American Nuclear Society*, vol. 23, 1976.

[2] V. Y. Gol'din, "A quasi-diffusion method of solving the kinetic equation," *USSR Computational Mathematics and Mathematical Physics*, vol. 4, pp. 136–149, 1964.

[3] E. W. Larsen, J. E. Morel, and W. F. Miller Jr., "Asymptotic solutions of numerical transport problems in optically thick, diffusive regimes," *J. Comput. Phys.*, vol. 69, no. 2, pp. 283–324, 1987.

[4] R. E. Alcouffe, "Diffusion synthetic acceleration methods for the diamond-differenced discrete-ordinates equations," *Nuclear Science and Engineering*, vol. 64, no. 2, pp. 344–355, 1977.

[5] M. L. Adams and E. W. Larsen, "Fast iterative methods for discrete-ordinates particle transport calculations," *Progress in Nuclear Energy*, vol. 40, no. 1, pp. 3–159, 2002.
[6] A. Szoke and E. D. Brooks III, "The transport equation in optically thick media," *Journal of Quantitative Spectroscopy and Radiative Transfer*, vol. 91, no. 1, pp. 95–110, 2005.
[7] F. Daffin, M. S. McKinley, E. D. Brooks, and A. Szoke, "An evaluation of the difference formulation for photon transport in a two level system," *Journal of Computational Physics*, vol. 204, no. 1, pp. 27–45, 2005.
[8] T. Luu, E. D. Brooks, and A. Szoke, "Generalized reference fields and source interpolation for the difference formulation of radiation transport," *Journal of Computational Physics*, vol. 229, no. 5, pp. 1626–1642, 2010.
[9] J. A. Fleck and J. D. Cummings, "An implicit monte carlo scheme for calculating time and frequency dependent nonlinear radiation transport," *J. Comput. Phys.*, vol. 8, pp. 313–342, 1971.
[10] J. A. Fleck and E. H. Canfield, "A random walk procedure for improving the computational efficiency of the implicit monte carlo method for nonlinear radiation transport," *J. Comput. Phys.*, vol. 54, pp. 508–523, 1984.
[11] N. Gentile, "Implicit monte carlo diffusion - an acceleration method for monte carlo time-dependent radiative transfer simulations," *J. Comput. Phys.*, vol. 172, pp. 543–571, 2001.
[12] M. A. Cleveland, N. A. Gentile, and T. S. Palmer, "An extension of implicit monte carlo diffusion: Multigroup and the difference formulation," *Journal of Computational Physics*, vol. 229, no. 16, pp. 5707–5723, 2010.
[13] J. D. Densmore, T. J. Urbatsch, T. M. Evans, and M. W. Buksas, "A hybrid transport-diffusion method for monte carlo radiative-transfer simulations," *Journal of Computational Physics*, vol. 222, no. 2, pp. 485–503, 2007.
[14] J. D. Densmore, K. G. Thompson, and T. J. Urbatsch, "A hybrid transport-diffusion monte carlo method for frequency-dependent radiative-transfer simulations," *Journal of Computational Physics*, vol. 231, no. 20, pp. 6924–6934, 2012.
[15] M. A. Cooper and E. W. Larsen, "Automated weight windows for global monte carlo particle transport calculations," *Nuclear Science and Engineering*, vol. 137, pp. 1–13, 2001.
[16] V. N. Novellino and D. Y. Anistratov, "Analysis of hybrid mc/deterministic methods for transport problems based on low-order equations discretized by finite volume schemes," *Transaction of American Nuclear Society*, vol. 130, 2024.
[17] J. Willert, C. T. Kelley, D. A. Knoll, and H. Park, "Hybrid deterministic/monte carlo neutronics," *SIAM Journal on Scientific Computing*, vol. 35, no. 5, pp. S62–S83, 2013.
[18] H. Park, D. A. Knoll, R. M. Rauenzahn, A. B. Wollaber, and J. D. Densmore, "A consistent, moment-based, multiscale solution approach for thermal radiative transfer problems," *Transport Theory and Statistical Physics*, vol. 41, no. 3-4, pp. 284–303, 2012.
[19] H. Park, J. Densmore, A. Wollaber, D. Knoll, and R. Rauenzahn, "Monte carlo solution methods in a moment-based scale-bridging algorithm for thermal radiative transfer problems: Comparison with fleck and cummings," in *Proceedings of the International Conference on Mathematics and Computational Methods Applied to Nuclear Science & Engineering (M&C 2013)*, Sun Valley, Idaho, May 5-9, 2013 2013.
[20] A. Q. Lam, T. S. Palmer, T. A. Brunner, and R. M. Vega, "A monte carlo thermal radiative transfer solver with nonlinear elimination," *Journal of Computational and Theoretical Transport*, vol. 52, no. 3, pp. 221–245, 2023.
[21] S. Pasmann, I. Variansyah, C. T. Kelley, and R. McClarren, "A quasi–monte carlo method with krylov linear solvers for multigroup neutron transport simulations," *Nuclear Science and Engineering*, vol. 197, no. 6, pp. 1159–1173, 2023.
[22] S. Olivier and T. S. Haut, "High-order finite element second moment methods for linear transport," *Nuclear Science and Engineering*, vol. 198, no. 6, pp. 1179–1214, 2024.
[23] P. A. Raviart and J. M. Thomas, "A mixed finite element method for 2-nd order elliptic problems," in *Mathematical Aspects of Finite Element Methods*, 1977, pp. 292–315.
[24] P. A. Raviart and J. M. Thomas, "Dual finite element models for second order elliptic problems," *Energy Methods in Finite Element Analysis*, pp. 175–191, 1979.
[25] J. Jim Douglas and T. Dupont, "Interior penalty procedures for elliptic and parabolic galerkin methods," *Computers & Mathematics with Applications*, vol. 12, no. 10, pp. 1337–1355, 1976.
[26] D. N. Arnold, F. Brezzi, B. Cockburn, and L. D. Marini, "Unified analysis of discontinuous Galerkin methods for elliptic problems," *SIAM Journal on Numerical Analysis*, vol. 39, no. 5, pp. 1749–1779, 2002.
[27] M. Pozulp, "A hybrid monte carlo-deterministic second moment method for thermal radiative transfer," PhD dissertation, University of California, Berkeley, Berkeley, CA, May 2025.
[28] M. Pozulp and T. Haut, "A proof of the asymptotic variance of estimators for monte carlo source iteration in the thick diffusion limit," 2026, preprint submitted to Elsevier. [Online]. Available: https://mike.pozulp.com/2026proof_of_var.pdf
[29] R. Anderson, J. Andrej, A. Barker, J. Bramwell, J.-S. Camier, J. Cerveny, V. Dobrev, Y. Dudouit, A. Fisher, T. Kolev, W. Pazner, M. Stowell, V. Tomov, I. Akkerman, J. Dahm, D. Medina, and S. Zampini, "Mfem: A modular finite element methods library," *Computers & Mathematics with Applications*, vol. 81, pp. 42–74, 2021.
[30] R. D. Falgout and U. M. Yang, "hypre: A library of high performance preconditioners," in *ICCS 2002*, pp. 632–641.
[31] X. S. Li, "An overview of superlu: Algorithms, implementation, and user interface," *ACM Trans. Math. Softw.*, vol. 31, no. 3, p. 302–325, sep 2005.
[32] P. Roache, *Verification and Validation in Computational Science and Engineering*. Hermosa Publishers, 1998.
[33] K. Salari and P. Knupp, "Code verification by the method of manufactured solutions," SAND2000-1444, Tech. Rep., 2000.
[34] P. J. Roache, "Code verification by the method of manufactured solutions," *Journal of Fluids Engineering*, vol. 124, no. 1, pp. 4–10, 11 2001.
[35] S. Olivier, W. Pazner, T. S. Haut, and B. C. Yee, "A family of independent variable eddington factor methods with efficient preconditioned iterative solvers," *Journal of Computational Physics*, vol. 473, p. 111747, 2023.
[36] F. Graziani and J. LeBlanc, "The crooked pipe test problem," UCRL-MI-143393, Tech. Rep., 2000.